3rd AIAA Flow Control Conference
5 - 8 June 2006; San Francisco, California

AIAA 2006-3701

Design Enhancements of the Two-Dimensional, Dual Throat Fluidic Thrust Vectoring Nozzle Concept

Jeffrey D. Flamm*, Karen A. Deere†, Mary L. Mason‡, Bobby L. Berrier§, and Stuart K. Johnson**
NASA Langley Research Center, Hampton, Virginia, 23681

A Dual Throat Nozzle fluidic thrust vectoring technique that achieves higher thrust-vectoring efficiencies than other fluidic techniques, without sacrificing thrust efficiency has been developed at NASA Langley Research Center. The nozzle concept was designed with the aid of the structured-grid, Reynolds-averaged Navier-Stokes computational fluidic dynamics code PAB3D. This new concept combines the thrust efficiency of sonic-plane skewing with increased thrust-vectoring efficiencies obtained by maximizing pressure differentials in a separated cavity located downstream of the nozzle throat. By injecting secondary flow asymmetrically at the upstream minimum area, a new aerodynamic minimum area is formed downstream of the geometric minimum and the sonic line is skewed, thus vectoring the exhaust flow. The nozzle was tested in the NASA Langley Research Center Jet Exit Test Facility. Internal nozzle performance characteristics were defined for nozzle pressure ratios up to 10, with a range of secondary injection flow rates up to 10 percent of the primary flow rate. Most of the data included in this paper shows the effect of secondary injection rate at a nozzle pressure ratio of 4. The effects of modifying cavity divergence angle, convergence angle and cavity shape on internal nozzle performance were investigated, as were effects of injection geometry, hole or slot. In agreement with computationally predicted data, experimental data verified that decreasing cavity divergence angle had a negative impact and increasing cavity convergence angle had a positive impact on thrust vector angle and thrust efficiency. A curved cavity apex provided improved thrust ratios at some injection rates. However, overall nozzle performance suffered with no secondary injection. Injection holes were more efficient than the injection slot over the range of injection rates, but the slot generated larger thrust vector angles for injection rates less than 4 percent of the primary flow rate.

* Aerospace Engineer, Configuration Aerodynamics Branch, Mail stop 499, 16 Victory St., NASA Langley Research, Hampton, Virginia, 23681, AIAA Associate Fellow.
† Aerospace Engineer, Configuration Aerodynamics Branch, Mail stop 499, 16 Victory St., NASA Langley Research, Hampton, Virginia, 23681, AIAA Senior Member.
‡ Aerospace Engineer, Configuration Aerodynamics Branch, Mail stop 499, 16 Victory St., NASA Langley Research, Hampton, Virginia, 23681.
§ Aerospace Engineer, Configuration Aerodynamics Branch, Mail stop 499, 16 Victory St., NASA Langley Research, Hampton, Virginia, 23681, AIAA Fellow.
** Aerospace Engineer, Advanced Aerospace Systems Branch, Mail stop 411, 16 Victory St., NASA Langley Research, Hampton, Virginia, 23681.

Nomenclature

A_t = nominal nozzle throat area, 4.6 in^2
A_e = nominal nozzle exit area, 4.6 in^2
A_{min} = nozzle minimum geometric area in^2 (see Figure 8)
A_{VC} = effective nozzle flow area decreased by vena contracta effects, in^2 (see Figure 8)
$C_{d,prim}$ = discharge coefficient of primary nozzle, $\frac{w_p + w_s}{w_{i,p}}$
$C_{fg\ sys}$ = system resultant thrust ratio, $\frac{F_r}{F_{i,p} + F_{i,s}}$
DTN = Dual Throat Nozzle
F_A = measured axial force, lbs
$F_{i,p}$ = ideal isentropic thrust of primary nozzle, lbs
$F_{i,s}$ = ideal isentropic thrust of secondary nozzle, lbs
F_N = measured normal force, lbs
F_r = resultant thrust, $\sqrt{F_A{}^2 + F_N{}^2 + F_S{}^2}$ lbs
F_S = measured side force, lbs
h_{ut} = height of primary nozzle upstream throat, 1.15 in. (see Figure 4)
h_{dt} = height of primary nozzle downstream throat, 1.15 in. (see Figure 4)
l = length of primary nozzle cavity, 3.0 in. (see Fig 4)
M = Mach number
NPR = nozzle pressure ratio, $\frac{p_{t,j}}{p_a}$
NPR_D = design nozzle pressure ratio
p = local static pressure, psi
p_a = atmospheric pressure, psi
$p_{t,j}$ = average total pressure of primary jet, psi
$p_{t,s}$ = measured total pressure of secondary jet, psi
$T_{t,j}$ = measured total temperature of primary jet, °R
$T_{t,s}$ = measured total temperature of secondary0 jet, °R
W = width of nozzle, 4.0 in.
$w_{i,p}$ = ideal weight flow rate of primary nozzle, lb/sec
w_p = measured weight flow rate of primary jet, lb/sec
w_s = measured weight flow rate of secondary jet, lb/sec
x, y, z = Cartesian coordinates
δ_p = resultant pitch thrust-vector angle, $\tan^{-1}\frac{F_N}{F_A}$, deg
η = resultant pitch thrust vectoring efficiency, $\frac{\delta_p}{w_s/(w_s + w_p)} * 100$, degrees / percent injection
θ_1 = upstream divergent cavity ramp angle, degrees (see Figure 4)
θ_2 = downstream convergent cavity ramp angle, degrees (see Figure 4)
ϕ = Secondary flow injection angle, degrees (see Figure 4)

I. Introduction

Fluidic injection for thrust-vector angle control and throat area control in exhaust nozzles has gained renewed interest over the last 10 years. Unlike mechanical thrust-vectoring nozzles that use actuated hardware to vector the primary jet thrust, fluidic thrust-vectoring nozzles use a secondary air stream to manipulate the primary jet flow.

Therefore, fixed geometry, fluidic thrust-vectoring nozzles potentially provide effective flow deflection, yet weigh less than their mechanical thrust vectoring counterparts.

Some of the primary mechanisms for thrust vector control include shock-vector control, sonic-plane skewing, and counterflow (refs. 1-13). The shock-vector control method (fluidic injection downstream of nozzle throat) offers substantial vector control, but often reduces thrust ratio (ref. 12). Fluidic sonic-plane skewing methods (fluidic injection at nozzle throat) typically produce higher thrust ratios, but lower resultant thrust vector angles than the shock-vector control method (ref. 11). The counterflow method (suction in a secondary duct between a primary exhaust nozzle and an aft collar) generates large vector angles with little secondary flow requirements, but issues such as suction supply source, hysteresis effects, and airframe integration need to be addressed (ref. 13).

A Dual Throat Nozzle (DTN) fluidic thrust vectoring technique that achieves higher thrust-vectoring efficiencies than other fluidic techniques without sacrificing thrust efficiency has been researched at NASA Langley Research Center (LaRC) (refs. 14, 15, 16). The DTN concept was designed with the aid of the structured-grid, Reynolds-averaged Navier-Stokes computational fluidic dynamics code PAB3D (refs. 14, 15). The DTN technique combines the thrust efficiency of sonic-plane skewing with increased vectoring efficiencies obtained by maximizing pressure differentials in a separated cavity located between two geometric minimum areas. The nozzle concept, shown in Figure 1, is a 2-dimensional convergent-divergent-convergent nozzle with two geometric minimum areas, denoted as "dual throats." A cavity is formed between the two minimum areas. A fluidic injection port is located at the upstream minimum area (on both the upper and lower surface for an actual application). Asymmetric injection of secondary flow (from a port on one side of the nozzle) at the upstream minimum area creates a new aerodynamic minimum area downstream of the geometric minimum. The sonic plane becomes skewed, vectoring the primary flow and forcing flow separation in the cavity located on the injection side. A recirculation area forms in the separated-flow cavity and thus, the wall pressures in that region are pumped down by the primary flow. Meanwhile the cavity on the opposite side of the secondary injection is filled by the high-pressure primary flow. The low pressure in one cavity coupled with the high pressure in the opposite cavity further vectors the flow. Therefore, thrust vectoring is further enhanced over the throat skewing alone concept by the presence of the cavity regions. Researchers at NASA LaRC have computationally guided the design (refs. 14 and 15) and experimentally demonstrated (ref. 16) a two-dimensional (2D), rectangular-shaped dual throat nozzle that achieves larger thrust vectoring efficiencies than the traditional throat shifting method, without large impact on system thrust ratio (Figure 2). Several CFD design and experimental validation cycles were completed.

To improve thrust vectoring performance, several new geometric configurations of the LaRC 2D rectangular dual throat nozzle were designed, analyzed computationally and tested at static flow conditions. The effect of convergent and divergent ramp angles, the effect of cavity shape, the effect of secondary injection hole size, and the effect of secondary injection geometry (row of holes or slot) on nozzle internal performance will be presented.

II. Apparatus and Experimental Methods

The study was conducted in the NASA Langley Research Center Jet Exit Test Facility. The following sections will discuss the test facility, dual-flow propulsion system, model hardware, test conditions, and data acquisition and reduction methods.

A. Jet Exit Test Facility

The Jet Exit Test Facility is an indoor reduced-scale pressurized-air test stand combining multi-flow propulsion simulation with high-pressure and high flow-rate capabilities. This facility is typically used to test nozzle internal performance at static (no external flow) conditions. A continuous supply of clean, dry high-pressure air is delivered from a central 5000-psi compressor station. The high-pressure supply is reduced to feed two independently controlled 1800-psi air lines which supply the test model. The air control system is similar to that of the Langley 16-Foot Transonic Tunnel (ref. 16) but has been enhanced by the installation of settling tanks after the 5000-psi reduction and by the addition of bypass regulation systems (for precise low-flow and high-flow settings) and dual flow-control valves after regulation. Pressurized air from one or both supply lines is directed through a single-engine simulation system to the test nozzle and vented to atmosphere in the large test bay area through two sets of acoustically-treated ceiling ducts. A photograph of a dual throat nozzle installed in the test facility is shown in Figure 3.

B. Dual-flow Propulsion Simulation System

The dual throat nozzle fluidic thrust vectoring nozzle model was tested on the facility dual-flow propulsion simulation system. The test rig is an axisymmetric single-engine propulsion simulator with dual co-annular ducts

mounted on a six-component strain-gauge balance (NASA 1636). An 1800-psi air line supplies each of the model plenums: the core flow (primary) plenum and the outer annular (secondary) plenum. Each supply line is instrumented with a multiple critical venturi system (ref. 17) capable of flow rates up to 25 lb/sec and incorporates a steam heat exchanger to maintain nozzle and secondary total temperatures near 75° F. In the simulator, the high-pressure air transitions from the non-metric to metric (supported by the balance) part of the test rig through semi-rigid, stainless-steel, 's' shaped tubes (S-tubes). The S-tubes (two per flow path) are designed to minimize the balance tares and axial momentum transfer caused by the high-pressure air crossing the metric/non-metric break on the test rig. The primary (nozzle) air supply passes from the core plenum to an annular duct located on the test-stand centerline through eight radially spaced sonic nozzles. The flow then passes through a circular duct, a transition section (round-to-rectangular) and a choke plate (flow-straightener) before entering the rectangular instrumentation section. From the instrumentation section, the flow then enters the primary nozzle. To supply the nozzle secondary injection plenum, the test rig nominal secondary flow path was blocked to pressurize the test rig secondary plenum. A high-pressure flexible hose was used to connect the test rig plenum to a remote-control valve located on the lower portion of the nozzle model. This valve provided final control of the air entry to the nozzle model secondary flow injection plenum.

C. Model Description

The model is a 2-D convergent-divergent-convergent primary nozzle with two geometric minimum areas. The design incorporates a cavity between the two minimum areas. The nozzle width was 4.0 in. The upstream and downstream nominal throat heights were $h_{ut} = h_{dt} = 1.15$ in. The nominal upstream and downstream throat areas were 4.6 sq in. Figure 4 presents a sketch of the model illustrating the geometric design variables presented in this paper. The cavity length tested was $l = 3.0$ in. for all configurations. The divergent cavity ramp angles tested were $\theta_1 = -10$ and -20 degrees. The convergent cavity ramp angles tested were $\theta_2 = 20$ and 30 degrees. Additionally, a curved cavity (with sketch shown in Figure 5 and coordinates presented in Table 2) was tested. The secondary flow was injected at the upstream minimum area. Three different secondary injection geometries were tested: a single row of "small holes," a single row of "large holes," and a slot. The small secondary flow injection holes had a diameter of 0.05 inches and were spaced 0.04 inches apart edge to edge (total of 44 injection holes) for a total open area = 0.0864 square inches. The large secondary flow injection holes had a diameter of 0.09 inches and were spaced 0.04 inches apart edge to edge (total of 30 injection holes) for a total open area = 0.1909 square inches. The slot injector had a total open area of 0.0864 square inches, equivalent to the "small hole" injector. The secondary flow injection angle, ϕ, was 150 degrees for all configurations presented.

D. Instrumentation

Forces and moments on the model were measured using a six-component strain gauge balance (NASA balance 1636). The maximum capacity and estimated accuracy for each balance component are listed in Table 1. Since the model was symmetric about the *x-y* and *x-z* planes (with the exception of the secondary injection ports), significant rolling moment, yawing moment, and side force measurements were not expected.

The model was instrumented with up to 68 surface static pressure taps on the centerline of the internal surface of the primary nozzle. The taps were spaced evenly every 0.10 inch starting at 0.20 inch upstream of the upstream-nozzle throat extending to the nozzle exit (or downstream throat). The model static pressures were measured using electronic pressure transducers with a range of either 100 psid or 250 psid, depending on maximum expected pressure levels. The accuracy of the electronic pressure transducers as given by the manufacturer was ±0.1 percent of full scale.

The primary jet total pressure, $p_{t,j}$, was obtained by mounting three rakes with a total of nine Pitot probes in the instrumentation section upstream of the primary nozzle. The pressures were measured by using electronic pressure transducers with a range of 250 psid with an accuracy ±0.1 percent of full scale. The nine individual readings were then averaged to obtain $p_{t,j}$. The primary jet total temperature, $T_{t,j}$, was measured by a single thermocouple also mounted in the instrumentation section. The accuracy of the thermocouple as given by the manufacturer was ±4 °F. The secondary air total pressure, $p_{t,s}$, was measured by a single Pitot probe located in the injection block plenum using an individual 500 psid pressure transducer with an accuracy of ±0.1 percent of full scale. The secondary total temperature, $T_{t,s}$, was measured by a single thermocouple located in the union between the flexible hose line feeding secondary air to the model and the injection block. The accuracy of the thermocouple as given by the manufacturer was ±2 °F. The ambient pressure, p_a, was measured with a 15 psia pressure transducer with an accuracy of ±0.03 percent of reading (sea-level barometric pressure).

The weight flow rate of the air supplied to the primary nozzle and the secondary injection block was measured by a pair of multiple critical venturi systems located upstream of a pair of S-tubes. The S-tubes were used to bridge the airflow from the non-metric to metric portion of the test hardware. The multiple critical venturi's have been calibrated to an accuracy of 0.1 percent of reading. Reference 17 describes the multiple critical venturi system in further detail.

E. Computational methods

The computational fluid dynamics (CFD) code PAB3D was used to guide the experimental nozzle design (refs. 14 and 15). PAB3D was chosen for this nozzle work because it was originally developed as an internal flow, propulsion code and now has been well tested and documented for predicting complex flow features in aeropropulsive, as well as aerodynamic configurations (refs. 17 to 27). The 2D computational domain used in references 14 and 15 simulated a 3D quasi-slot configuration without the effects of viscous sidewalls, while the experimental models used a row of injection holes and of course, had viscous sidewall effects. Therefore, as expected, PAB3D did not predict absolute magnitudes of the slightly different experimental geometry, but predicted trends in nozzle performance and thrust vectoring efficiency quite well (ref. 15). PAB3D proved to be a valuable resource for screening a multitude of geometric parameters in an effort to down select critical parameters to validate experimentally.

PAB3D requires a structured-mesh computational domain. A multiblock (ref. 18) feature allows the domain to be partitioned into sections, which is critical for modeling complex configurations and for efficiently running the parallel version of PAB3D. The implicit, finite-volume flow solver represents the three-dimensional (3D), unsteady Reynolds-averaged Navier-Stokes (URANS) equations. Several advanced turbulence models (refs. 28 to 31) are available for closure of the URANS equations. All solutions were computed with nonlinear k-e turbulence model of Girimaji. PAB3D is second order time-accurate and has the capability to simulate time-varying boundary conditions (refs. 32 and 33). Details of the computational study used to guide selection of the experimental test parameters can be found in the companion papers to this one (refs. 14 and 15). Solutions were deemed converged when thrust vector angle varied less than 0.5°, and primary discharge coefficient and system thrust ratio varied less than 0.5%, over several thousand iterations. Solution residuals were monitored and a drop of at least 2 orders of magnitude was desired for the solution to be considered converged.

F. Computational Domain

The 2D computational structured-grid mesh used in the current paper simulated a 3D quasi-slot configuration without the effects of viscous sidewalls. The computational mesh modeled an injection plenum and an injection opening angled at 150° upstream. The 2D mesh had only one cell in the third dimension with symmetric boundary conditions used on lateral faces, such that the flow would be representative of flow along the centerline of the 3D experimental model with the slot injection and plenum. Nozzle surfaces were simulated with an adiabatic, no-slip wall boundary condition for viscous effects. The nozzle inlet conditions were set with a total temperature and total pressure boundary condition. Riemann invariants along the characteristics were used for the upstream, upper and lower far field boundary conditions. A subsonic, constant pressure outflow boundary condition, which automatically switches to first order extrapolation if the flow Mach number is supersonic, was used along the downstream far field boundary.

Grid sequencing was used to evaluate grid convergence. Solutions were initially run on coarse, medium and fine meshes. When very small changes in internal nozzle performance parameters and thrust vector angles were acquired between the medium and fine mesh solutions, the medium mesh was deemed more than sufficient for estimating performance trends and often adequate for predicting performance magnitudes.

III. Results and Discussion

A. Nozzle performance without secondary injection

Figure 6 presents the experimental nozzle performance for primary flow without secondary fluidic injection for all geometric configurations. While the data presented in Figure 6 is without secondary flow injection, the nozzle was run with the secondary injection blocks installed and valved closed to prevent flow entrainment from the secondary airline. Since three different secondary injection geometries were tested, small holes, large holes and slot, they imposed different geometric disturbances at the upstream throat. The effect of secondary injection type is further discussed in section E below. Resultant pitch vector angle (δ_p), resultant thrust ratio ($C_{fg\ sys}$), an indicator of thrust efficiency, and nozzle primary-flow discharge coefficient ($C_{d,prim}$) are presented as functions of primary nozzle pressure ratio (NPR). As expected with no secondary flow, changes in nozzle geometry have little effect on

resultant pitch vector angle. Resultant pitch vector angle is offset from zero by approximately 1 degree depending on NPR. The slight offset in pitch angle likely reflects an asymmetry in the flow through the nozzle upstream throat caused by the presence of secondary injection holes on the lower portion of the nozzle.

As observed in previous testing (ref. 16), the nozzle thrust ratio, $C_{fg,sys}$, typically peaked between 0.975 and 0.980 at NPR = 3 instead of peaking near NPR_D =1.89 for a typical convergent nozzle. The configuration with θ_1 =-20°, θ_2 = 20°, thrust ratio, $C_{fg,sys}$, peaked at approximately 1 to 1.5 percent lower than the other geometries tested. The larger magnitude of divergent ramp angle (θ_1 =-20°) probably resulted in larger internal flow separation and thrust losses not generated by the θ_1 =-10° configurations. As NPR continues to increase, $C_{fg,sys}$, decreases almost linearly to approximately 0.925 as the nozzle becomes highly under-expanded.

The nozzle discharge coefficient, $C_{d,prim}$, showed a small variation for the three configurations with θ_1 =-10°, θ_2 = 20°. The differences are likely due to the different disturbances at the throat caused by the different injection geometries. The θ_1 =-10°, θ_2 = 30° case was approximately 1 percent lower in discharge coefficient than the θ_1 =-10°, θ_2 = 20° cases at NPR = 2. The penalty in discharge coefficient decreased as NPR increased. The curved cavity and the θ_1 =-20°, θ_2 = 20°cavity both showed significant reductions in discharge coefficient at all NPR's compared to the θ_1 =-10°, θ_2 = 20°configurations, approximately 1% and 2% respectively. As observed previously for variations in cavity length (ref. 16), for all cavity shapes tested without secondary injection, the upper and lower cavities were partially separated. The losses in discharge coefficient can be attributed to internal separation and vena contracta losses, which will be discussed below.

Figure 7 presents a comparison of primary-flow experimental and computational (CFD) discharge coefficient ($C_{d,prim}$) and resultant thrust ratio ($C_{f,g\ sys}$) as a function of NPR for the baseline θ_1 =-10°, θ_2 = 20° nozzle geometry. While there was generally good agreement between the predictions and experimental data, the computational $C_{d,prim}$ results are lower than the experimental $C_{d,prim}$ results over the NPR range tested. Lower discharge coefficient levels for the computational results can be attributed to vena contracta effects or differences between the computational mesh and the as-built test article. The computational $C_{f,g\ sys}$ results fall below the experimental results at lower NPR but increase to better agreement at NPR = 7.

A computational prediction of internal pressure just below NPR = 5.0 for the baseline θ_1 =-10°, θ_2 = 20° nozzle geometry without injection is presented in figure 8 to illustrate the vena contracta concept. Without fluidic injection, the dual throat nozzle has a lower discharge coefficient than a well-designed non-vectoring convergent or convergent-divergent nozzle, which may be as high as 0.98 or 0.99. A discharge coefficient less than 1 indicates that the actual flow rate is less than the ideal flow rate for a given area. The vena contracta effect occurs when the flow along the walls at the upstream throat cannot manipulate the turn and overshoots the angle resulting in an effective area smaller than the actual geometric area. Figure 8(b) shows an enlarged view of the total pressure contours at the upstream throat. The geometric minimum area, A_{min}, is larger than the area of high total pressure flow (red contours) restricted through the vena contracta effect. Thus, the reduced actual flow area from the vena contracta effect (A_{vc}) caused lower discharge coefficients than if the vena contracta effect was absent from the flow.

B. Effect of cavity divergence angle with secondary injection

Figure 9 shows the variation of nozzle internal performance for two divergent cavity ramp angles θ_1 as a function of secondary weight-flow ratio at NPR = 4. In agreement with computational predictions presented in reference 15, experimental results verify that decreasing θ_1 from -10 to -20 degrees significantly decreases the resultant pitch thrust vector angle (δ_p) over the range of secondary weight flow ratios tested. At 3% secondary injection, thrust vector angle decreased from δ_p= 11.6° for θ_1 =-10° to δ_p=7.0 ° for θ_1 = -20. Thrust ratio (or thrust efficiency), $C_{f,g\ sys}$, follows similar trends for the two configuration, decreasing with increasing secondary injection rate. However, $C_{f,g\ sys}$ for the θ_1 = -20° case is significantly lower than that of θ_1 = -10° at all secondary injection rates tested. At 3% secondary injection $C_{f,g\ sys}$ is reduced by approximately .019 compared with the θ_1 = -10° configuration. Similarly, discharge coefficient, $C_{d,prim}$ follows similar trends for the two cases decreasing with increasing secondary injection rate. Again the θ_1 = -20° case has a slightly lower discharge coefficient than that of the θ_1 = -10° case. At 3% secondary injection $C_{d,prim}$ is reduced by approximately .013 compared with the θ_1 = -10° configuration. Figure 10 presents the experimental centerline pressures for two convergent cavity ramp angles θ_1, at NPR = 4 and 3% secondary injection. The lower surface centerline pressure distributions for the two configurations are similar. The curve is flat where the flow is separated along the lower cavity wall, and there is a slight increase in pressure near the nozzle exit as the primary jet vectors down and impinges on the lower surface. The upper surface pressures distribution for θ_1 =-10° indicates lower pressure just downstream of the first throat (x/l = 0.0) and higher pressure in the upper cavity at x/l > .35 than that of the θ_1 =-20° case. To provide insight into the internal flow

characteristics, figure 11 presents an experimental shadowgraph image and computational Mach contours for the θ_1 = -10°, θ_2 = 20° configuration at NPR = 4 with 3% secondary injection. Figure 12 presents computational Mach contours for the θ_1 = -20°, θ_2 = 20° configuration at NPR = 4 with 3% secondary injection. The computational Mach number contours and experimental shadowgraph images indicate that the primary jet flow is attached to the upper cavity for θ_1 =-10°, while the primary jet is likely separated from the upper cavity for θ_1=-20°. Therefore, resultant pitch thrust vector angle decreases with increasing magnitude divergent ramp angle (negative angle) because the pressure differential between the upper and lower nozzle cavities is reduced as the flow separates from both cavity walls for θ_1 = -20°.

C. Effect of cavity convergence angle with secondary injection

Figure 13 presents the experimental nozzle internal performance data for two convergent ramp angles (θ_2) as a function of secondary weight-flow ratio at NPR = 4. Increasing θ_2 from 20 to 30 degrees increased the resultant pitch thrust vector angle over the range of secondary weight flow ratios tested. At 3% secondary injection, thrust vector angle increased from δ_p= 11.6° for θ_2 = 20° to δ_p= 15.1° for θ_2 = 30°. Thrust vectoring efficiency, η, was 5 degrees per percent secondary injection for the θ_2 = 30° case. Thrust ratio, $C_{f,g\ sys}$, follows similar trends for both configurations decreasing with increasing secondary injection rate for the two configurations. However, $C_{f,g\ sys}$ for the θ_2 = 30° case is slightly lower than that of θ_2 = 20°. At 3% secondary injection $C_{f,g\ sys}$ is reduced by approximately .007 compared with the θ_2 = 20° configuration. Discharge coefficient, $C_{d,prim}$, also follows similar trends for the two cases decreasing with increasing secondary injection rate. The θ_2 = 30° case has a slightly lower discharge coefficient than that of the θ_2 = 20° case. At 3% secondary injection $C_{d,prim}$ is reduced by approximately .012 compared with the θ_2 = 20° configuration. The main objective of the design of this nozzle was to maximize resultant pitch thrust vector angle and pitch vectoring efficiency with minimal impact on other nozzle performance parameters. The configuration with θ_2 = 30° achieved this goal with only small impacts on thrust efficiency and discharge coefficient.

Experimental centerline pressures are shown in Figure 14. The lower surface centerline pressure distributions for the two configurations are generally similar. The curve is flat where the flow is separated along the lower cavity wall, and there is a slight increase in pressure near the nozzle exit as the primary jet vectors down and impinges on the lower surface. The upper surface pressure distributions for the two configurations follow similar trends until x/l of approximately 0.75. At this point (x/l=0.75), the cavity begins to converge and the θ_2 = 30° configuration shows an increase in pressure, thus accounting for the increased resultant pitch thrust-vector angle compared to the θ_2 =20° case.

A comparison of experimental pressure data with computational prediction for the θ_2=30° configuration is shown in Figure 15. A comparison of experimental pressure data with computational prediction for the θ_2=20° configuration is presented in Figure 16 and will be discussed in further detail in section E. The computational predictions were generally in good agreement with experimental measurements.

The comparison of nozzle internal performance for experimental data with computational prediction for cavity convergence angles of 20° and 30° is shown in Table 3. Both experimental data and computational predictions indicated an improvement in thrust vector angle and efficiency at NPR=4 with 3% injection as cavity convergence angle increased from 20° to 30°. PAB3D predicted the general trends in nozzle performance and specifically predicted the magnitude of thrust vector angle within less than 1° and thrust vectoring efficiency within 0.25°/%-injection. For computational results, good predictions of discharge coefficient and thrust ratio would typically fall within 0.5% of experimental data for less complicated nozzles than this one (i.e. without large separated flow regions). For this data, CFD over-predicted the restriction of the primary flow by the secondary, resulting in a smaller effective area and smaller discharge coefficient than the experiment. System thrust ratio was within .3% of experimental data both the θ_2=20° and θ_2=30° configurations. . Since experimental data was limited to cavity convergence angles of θ_2=20° and θ_2=30°, CFD was used to predict the trend up to 40°. Computational results indicated a decrease in all performance parameters as cavity convergence angle was increased from 30° to 40°.

Figure 11 introduced in section B, and Figure 17 show the comparison of experimental shadowgraph with computational Mach contours for cavity convergence angles of θ_2=20° and θ_2=30°, respectively, at NPR = 4 and 3% secondary injection. As expected from earlier agreement between experimental performance data and CFD predictions, the experimental and computational flow patterns are remarkably similar for each configuration. Visible in both the shadowgraph and the computational Mach contours are the lamba foot on the upper divergent cavity wall with a strong shock to subsonic flow, flow separation in the upper cavity apex, massive flow separation along the lower cavity walls, and plume flow expansion to supersonic flow. The shadowgraph for the θ_2=30°

configuration (figure 17) shows a Mach disk approximately one cavity length downstream of the nozzle exit as the flow adjusts to ambient pressure. Evidence of a Mach disk appears to be present for the θ_2=20° case (figure 11), although the focus is not as sharp and obvious as the θ_2=30° configuration. Comparison of the flow contours for the θ_2=20° with those of the θ_2=30° configuration, the lambda foot and strong shock on the upper divergent cavity wall move upstream and there is more cavity apex separation for the θ_2=30° configuration. Sonic flow in the computational flow contours is represented with a black line. The upstream sonic flow "throat" of the θ_2=30° geometry is skewed to a larger angle. As a result, the experimental thrust vector angle for the θ_2=30° configuration increases to a value of 15.128° , compared to a value of 11.888° for the with the θ_2=20° configuration despite the larger separated flow region in the upper cavity.

D. Effect of cavity shape with secondary injection

A nozzle with a curved contoured cavity was tested to verify the hypothesis that a contoured cavity apex could improve thrust efficiency compared to a sharp apex corner, while preserving thrust vectoring efficiency (figures 4 and 5). The sharp apex corner is located between straight cavity divergent and convergent ramps. The lower surface for the curved cavity contour is defined by coordinates presented in Table 2. The upper and lower cavities are symmetric. Since the sharp corner apex cavity with θ_1 =-10° and θ_2 = 30° generally achieved better thrust vector angles in the computational studies than the θ_1 =-10° and θ_2 = 20° configuration, the contour of the curved cavity was constrained to match the upstream throat and exit as well as the divergent and convergent ramp angles near the throat and and exit respectively of the θ_1 =-10° and θ_2 = 30° sharp corner apex configuration. A hyperbole was fit between these points to define the curved cavity.

Figure 18 shows a comparison of nozzle internal performance for the curved cavity shape configuration compared to the two sharp apex configurations (θ_1 =-10, θ_2 = 20° and θ_1 =-10, θ_2 = 30°). In general, the curved cavity performed the same as the sharp apex corner configuration with θ_1 =-10 and θ_2 = 30° at secondary injection rates less than or equal to 3%. As secondary injection rates increased above 3%, the curved cavity maintained similar vectoring performance as the θ_1 =-10 and θ_2 = 30°case, while improving thrust efficiency, $C_{f,g\ sys}$, to more closely match the θ_1 =-10 and θ_2 = 20° case. At 6% secondary injection, resultant pitch thrust vector angle was δ_p = 14.9° for the sharp apex θ_1 =-10 and θ_2 = 20° configuration, δ_p = 18.2° for the sharp apex θ_1 =-10 and θ_2 = 30° configuration, and δ_p = 18.6° for the curved apex configuration, while thrust efficiency was $C_{f,g\ sys}$ = .940 (θ_1 =-10 and θ_2 = 20°), $C_{f,g\ sys}$ = 0.936 (θ_1 =-10 and θ_2 = 30°), and $C_{f,g\ sys}$ =.940 (curved apex). At 8% secondary injection, the curved cavity achieved a δ_p = 19.3° , compared with δ_p = 17.9° for the sharp corner apex θ_1 =-10° and θ_2 = 30° configuration, while maintaining similar thrust efficiencies.

Figure 19 presents the nozzle centerline pressure distributions for the three cavity geometries tested at NPR=4 for several secondary injection rates. At 3% secondary injection (Figure 19(a)), the upper and lower surface pressure ratio distributions for each configuration are generally identical. Except for the θ_1 =-10° and θ_2 = 20° geometry, which produced lower pressures along the upper surface at x/l ≥ 0.75, indicative of the generally lower thrust vector angles achieved by this configuration. As secondary injection rate is increased to 6% (Figure 19(b)) and 8% (Figure 19(c)), the lower surface pressure distributions for all three configurations again follow similar trends. Along the upper surface, however, the curved cavity configuration produced higher pressure ratios upstream of the inflection point at approximately x/l = 0.80. To provide insight into the complex characteristics of the nozzle internal flow, Figure 20 presents shadowgraph flow visualizations. Figure 20 (a) shows the shadowgraph image of the θ_1 =-10° and θ_2 = 30° configuration at NPR = 4 with 6% secondary injection. Figure 20 (b) presents the image for the curved-cavity configuration at the same test conditions. Examining the shock patterns inside the nozzle as the primary flow turns through the apex of the cavity indicates slightly weaker shocks in the curved cavity configuration, which may account for the improved system thrust ratios.

The curved cavity and the straight ramped cavity, θ_1 =-10° and θ_2 = 30°, generally performed similarly in terms of thrust vector angle and system thrust ratio at secondary injection rates of 3% or less. At secondary injection rates above 3%, the curved cavity achieved pitch thrust vector angles the same or slightly better (1.5 degrees at 8 % secondary injection), while maintaining the superior thrust efficiency of the θ_1 =-10° and θ_2 = 20° configuration. However, as indicated in section A, the curved cavity suffered from significant penalty in discharge coefficient with no secondary flow.

E. Effect of secondary injection geometry

The test hardware in prior work (ref. 16) and in the current experiment was designed to inject secondary flow through a row of holes. Geometric variables for the current experiment included two different injection hole sizes and an open injection slot. Figure 21 presents the effect of injection geometry on nozzle internal performance at NPR =4. Performance parameters are again presented as functions of secondary weight-flow ratio. With fluidic injection rates less than 3% of the primary flow rate ($w_s/(w_s+w_p)$ = 0.03), the slot injector generated the largest vector angles while the large -area injection holes generated the lowest vector angles. However, at higher injection rates the effectiveness of the slot injector decreased and the small injection hole geometry achieved the highest vector angles.

The injection slot data is used to quantify the ability of the computational method, using 2D structured-grid Reynolds-Averaged Navier-Stokes flow solutions, to predict flow in the complex 3D DTN configurations and to quantify the differences between hole and slot injection. For computational ease, a 2D mesh was implemented for all of the rectangular DTN simulations. Figure 22 shows the comparison of experimental slot injection data with computational (CFD) predictions using the 3D quasi-slot for NPR=4 with no injection and with 3 and 6 percent injection. The good agreement of the experimental data with the CFD predictions indicates that a 2D mesh without viscous sidewalls, which simulates a 3D quasi-slot injection geometry, can predict trends and also give a good prediction of the magnitude of performance parameters. PAB3D with a 2D mesh is therefore an excellent screening tool that conserves computational resources, allows quick solution turn-around and produces good engineering predictions of nozzle performance. Thrust vectoring angle was predicted within less than 1°, while discharge coefficient and system thrust ratio predictions fell within 0.5% of experimental data. Two main differences between experimental data and computational predictions are the absence of the viscous sidewalls for all computational simulations and the absence of the plenum and injection opening in the no injection simulations. The later explains the 0.8° discrepancy in thrust vector angle, with the computational prediction of δ_p=0° for the perfectly symmetric configuration and δ_p=-0.8° for the experimental asymmetric geometry, which had the injection opening present, but not flowing, for the no injection case.

Figure 16 (introduced in section C) shows a comparison of the 2D quasi-slot computational prediction with pressure data for the 3D experimental slot and hole configurations for NPR=4 with a 3%-injection rate. Experimental data shown in Figure 21 indicates a 1-2 degree difference in thrust vector angle between the slot and hole injection techniques for NPR=4 with 3%-injection. The most obvious differences between slot and hole injection is the flow expansion and shock location on the upper wall, and the pressures along the lower wall are pumped down to a lower pressure with the slot injection. PAB3D did a fairly good job predicting the flow characteristics of the 3D slot injection along the upper wall, although the shock was slightly stronger and not in the exact location of the experiment. PAB3D was not able to predict the low pressures in the separated flow region along the lower wall. This data comparison between injection slots and holes was important to gather, in that all previous 2D computations used the "quasi-slot" in attempt to predict solution for a 3D injection hole configuration. So, the previous inability of the computational code to predict experimental data indicated either differences in injection geometry or shortcomings of the code or turbulence model. Now it is understood that it is a combination of the code having difficulty predicting pressures in a large separated flow region, which is common for many flow solvers, and that a 2D quasi-slot geometry is good for engineering estimates and screening geometric changes, but flow solutions with hole injection patterns cannot be completely predicted with a 2D quasi-slot geometry.

Since the 2D computational method predicts the nozzle performance and thrust vectoring of the experimental configuration with the injection slot, the differences seen between the experimental slot and hole data represent differences that may be expected when trying to use the computational method for an experimental hole injection pattern. This information is also enlightening when trying to understand the differences in magnitude between previous computational (2D quasi-slot injection) and experimental (hole injection) work shown in references 14 and 15. The primary cause for those differences in magnitude of nozzle performance and thrust vectoring for experimental and computational data now appears to be injection geometry. However, the computational method is very successful at predicting magnitudes in nozzle performance for slot injection geometric configurations and for predicting trends in performance for different (hole) injection schemes. Therefore, in an effort to screen configurations for further experimental validation, 2D PAB3D simulations are suitable for predicting trends in performance of experimental configurations with a row of injection holes to save CFD resources and time.

IV. Conclusion

A new fluidic thrust-vectoring technique that achieves higher thrust-vectoring efficiencies than other fluidic techniques documented in open literature, without large thrust efficiency penalties for vectoring operation has been developed at NASA Langley Research Center. This new concept combines the thrust efficiency of sonic-plane skewing with increased thrust-vectoring efficiencies obtained by maximizing pressure differentials in a separated cavity located downstream of the nozzle throat. By injecting secondary flow asymmetrically (from an injection port on one side of the nozzle) at the upstream minimum area, a new aerodynamic minimum area is formed downstream of the geometric minimum and the sonic line is skewed, thus vectoring the exhaust flow. The computational flow solver, PAB3D, was used extensively to guide the design of this dual throat nozzle and computational results have been published in several references. This paper documents the experimental data of key geometric parameters of the dual throat nozzle. The nozzle was tested in the NASA Langley Research Center Jet Exit Test Facility. The results from this investigation have indicated the following conclusions:

1. In agreement with computational prediction, experimental data verifies that increasing the magnitude of the divergent cavity ramp angle (negative angle) has a negative effect on overall performance, decreasing both pitch vectoring and resultant thrust ratios with secondary flow. Thrust ratio and nozzle discharge coefficient are also reduced without secondary flow.
2. In agreement with computational prediction, experimental data verifies that increasing convergent cavity ramp angle has a positive effect on resultant pitch thrust-vector angle, δ_p, and resultant pitch thrust vectoring efficiency, η.
3. The curved cavity had the lowest thrust ratio and nozzle discharge coefficients of any configuration tested without secondary flow (non-vectoring operation).
4. The curved cavity and the straight ramped cavity, θ_1 =-10° and θ_2 = 30°, generally performed similarly in terms of δ_p and $C_{f,g\ sys}$ at secondary injection rates of 3% or less, but the curved cavity achieved pitch vector angles slightly better (1.5 degrees at 8 % secondary injection) than the θ_1 =-10° and θ_2 = 30° configuration while maintaining the superior thrust efficiency of the θ_1 =-10° and θ_2 = 20° configuration at secondary injection rates above 3%.
5. Experimental data indicates a 1-2 degree difference in thrust vector angle between the slot and hole injection techniques for NPR=4 with 3%-injection. The most obvious differences between slot and hole injection are the flow expansion and shock location on the upper wall, and the pressures along the lower wall are pumped down to a lower pressure with the slot injection.
6. The computational method was able to predict the trends in thrust vector angle and nozzle internal performance. The computational method often predicted the magnitude of thrust vector angle to within less than 1° and discharge coefficient and system thrust ratio to less than 0.5 percent.
7. The 2D quasi-slot computational mesh provided a good engineering estimate of 3D experimental configuration with a row of holes used for the secondary injection. The prediction was improved when the 2D quasi-slot computational mesh was used to model flow through a 3D experimental slot injection.

References

[1]Anderson, C. J.; Giuliano, V. J.; and Wing, David J.: Investigation of Hybrid Fluidic / Mechanical Thrust Vectoring for Fixed-Exit Exhaust Nozzles. AIAA 97-3148, July 1997.

[2]Giuliano, V. J.; and Wing, David J.: Static Investigation of a Fixed-Aperture Exhaust Nozzle Employing Fluidic Injection for Multiaxis Thrust Vector Control. AIAA 97-3149, July 1997.

[3]Waithe, Kenrick A.: An Experimental and Computational Investigation of Multiple Injection Ports in a Convergent-Divergent Nozzle for Fluidic Thrust Vectoring. Master of Science Thesis, May 2001.

[4]Deere, Karen A., and Wing, David J.: PAB3D Simulations of a Nozzle with Fluidic Injection for Yaw-Thrust-Vector Control. AIAA 98-3254, July 1998.

[5]Hunter, C.A. and Deere, Karen A.: Computational Investigation of Fluidic Counterflow Thrust Vectoring. AIAA 99-2669, June 1999.

[6]Deere, K. A.: Computational Investigation of the Aerodynamic Effects on Fluidic Thrust Vectoring. AIAA 2000-3598, July 2000.

[7]Wing, David J.: Static Investigation of Two Fluidic Thrust-Vectoring Concepts on a Two-Dimensional Convergent-Divergent Nozzle. NASA TM-4574, December 1994.

[8]Wing, David J.; and Giuliano, V. J.: Fluidic Thrust Vectoring of an Axisymmetric Exhaust Nozzle at Static Conditions. ASME FEDSM97-3228, June 1997.

[9]Federspiel, J., Bangert, L., Wing, D.: Fluidic Control of Nozzle Flow - Some Performance Measurements. AIAA 95-2605, July 1995.

[10]Miller, D. N.; Yagle, P. J.; and Hamstra, J. W.: Fluidic Throat Skewing for Thrust Vectoring in Fixed Geometry Nozzles. AIAA 99-0365, January 1999.

[11]Yagle, P. J., Miller, D. N., Ginn, K. B.; and Hamstra, J. W.: Demonstration of Fluidic Throat Skewing for Thrust Vectoring in Structurally Fixed Nozzles. 2000-GT-0013, May 8-11, 2000.

[12]Deere, K. A.: Summary of Fluidic Thrust Vectoring Research Conducted at NASA Langley Research Center. AIAA-2003-3800, June 2003.

[13]Flamm, J. D.: Experimental Study of a Nozzle Using Fluidic Counterflow for Thrust Vectoring. AIAA 98-3255, July 1998.

[14]Deere, K. A.; Berrier, B. L.; Flamm, J. D.; and Johnson, S. K.: Computational Study of Fluidic Thrust Vectoring Using Separation Control in a Nozzle. AIAA-2003-3803, June 2003.

[15]Deere, K. A.; Berrier, B. L.; Flamm, J. D.; and Johnson, S. K.: A Computational Study of a Dual Throat Fluidic Thrust Vectoring Nozzle Concept. AIAA-2005-3502, July 2005.

[16]Flamm, J. D.; Deere, K. A.; Berrier, B. L.; and Johnson, S. K.; Mason, M. L.: Experimental Study of a Dual Throat Fluidic Thrust Vectoring Nozzle Concept. AIAA-2005-3503, July 2005.

[17]Abdol-Hamid, K. S.: The Application of 3D Marching Scheme for the Prediction of Supersonic Free Jets. AIAA 89-2897. July 1989.

[18]Abdol-Hamid, K. S.: Application of a Multiblock/ Multizone Code (PAB3D) for the Three-Dimensional Navier-Stokes Equations. AIAA-91-2155, June 1991.

[19]Carlson, J. R.: A Nozzle Internal Performance Prediction Method. NASA TP 3221, October 1992.

[20]Carlson, J. R.: Computational Prediction of Isolated Performance of an Axisymmetric Nozzle at Mach Number 0.90. NASA TM 4506, February 1994.

[21]Pao, S. P., Carlson, J. R., and Abdol-Hamid, K. S.: Computational Investigation of Circular-to-Rectangular Transition Ducts. Journal of Propulsion and Power, Vol. 10, No. 1, p 95-100, Jan.-Feb. 1994.

[22]Abdol-Hamid, K. S.; Lakshmanan, B.; and Carlson, J. R.: Application of Navier-Stokes Code PAB3D With k-ε Turbulence Model to Attached and Separated Flows. NASA TP-3480, January 1995.

[23]Abdol-Hamid, K. S., Carlson, J. R., and Pao, S. P.: Calculation of Turbulent Flows Using Mesh Sequencing and Conservative Patch Algorithm. AIAA 95-2336, July 1995.

[24]Pao, S. P.; and Abdol-Hamid, K. S.: Numerical Simulation of Jet Aerodynamics Using the Three-Dimensional Navier-Stokes Code PAB3D. NASA TP 3596, September 1996.

[25]Abdol-Hamid, K. S.; Lakshmanan, B.; and Carlson, J. R.: Application of Navier-Stokes Code PAB3D With k-ε Turbulence Model to Attached and Separated Flows. NASA TP-3480, January 1995.

[26] Carlson, J. R.: Applications of Algebraic Reynolds Stress Turbulence Models Part 1: Incompressible Flat Plate. Journal of Propulsion and Power, Vol. 13, No. 5, p 610-619, Sept.-Oct. 1997.

[27]Abdol-Hamid, K., Pao, S., Massey, S., and Elmiligui, A.: Temperature Corrected Turbulence Model for High Temperature Jet Flow. ASME Journal of Fluids Engineering, Vol. 126, No. 5, September 2004.

[28]Balakrishnan, L.; and Abdol-Hamid, K. S.: A Comparative Study of Two Codes with an Improved Two-Equation Turbulence Model For Predicting Jet Plumes. AIAA 92-2604, June 1992.

[29]Girimaji, S. S.: Fully-Explicit and Self-Consistent Algebraic Reynolds Stress Model. Inst. For Computer Applications in Science and Engineering, 95-82, December1995.

[30]Abdol-Hamid, K. S.: Implementation of Algebraic Stress Models in a General 3-D Navier-Stokes Method (PAB3D). NASA CR-4702, 1995.

[31]Abdol-Hamid, K. S. and Girimaji, S. S.: A Two-Stage Procedure Toward the Efficient Implementation of PANS and Other Hybrid Turbulence Models. NASA/TM-2004-213260, August 2004.

[32]Massey, S. J.; and Abdol-Hamid, K. S.: Enhancement and Validation of PAB3D for Unsteady Aerodynamics. AIAA 2003-1235, January 2003.

[33]Elmiligui, A., Abdol-Hamid, K., and Hunter, C.: Numerical Investigation of Flow in an Over-expanded Nozzle with Porous Surfaces. AIAA 2005-4159, July 2005.

Component	Balance Maximum	Max error	Max error as percentage of Balance Maximum
Normal	800 lbs	0.56 lbs	0.07
Axial	1200 lbs	2.38 lbs	0.20
Pitch	12000 in-lbs	17.64 in-lbs	0.15
Roll	1000 in-lbs	1.63 in-lbs	0.16
Yaw	12000 in-lbs	26.07 in-lbs	0.22
Side	800 lbs	0.47 lbs	0.06

Table 1. Balance accuracy.

X (in.)	Y (in.)	Z (in.)
-0.310	0.000	-0.715
-0.218	0.000	-0.662
-0.125	0.000	-0.608
-0.043	0.000	-0.579
0.043	0.000	-0.579
0.152	0.000	-0.598
0.261	0.000	-0.617
0.370	0.000	-0.636
0.482	0.000	-0.656
0.595	0.000	-0.676
0.707	0.000	-0.696
0.820	0.000	-0.715
0.932	0.000	-0.735
1.044	0.000	-0.755
1.157	0.000	-0.774
1.269	0.000	-0.794
1.382	0.000	-0.813
1.494	0.000	-0.832
1.607	0.000	-0.851
1.719	0.000	-0.870
1.832	0.000	-0.888
1.945	0.000	-0.904
2.058	0.000	-0.919
2.172	0.000	-0.928
2.285	0.000	-0.924
2.396	0.000	-0.896
2.501	0.000	-0.851
2.602	0.000	-0.799
2.702	0.000	-0.744
2.802	0.000	-0.688
2.901	0.000	-0.632
3.000	0.000	-0.575

Table 2. Lower Surface definition of curved cavity configuration.

	θ_2	δ_p	$C_{d,prim}$	$C_{f,gsys}$	η
Experiment	20	11.888°	0.8763	0.9574	3.978
Experiment	30	15.128°	0.8656	0.9553	5.024
CFD	20	11.38°	0.8596	0.9546	3.86
CFD	30	12.37°	0.8440	0.9523	4.12
CFD	40	11.64°	0.8353	0.9499	3.83

Table 3. Comparison of computational (CFD) nozzle performance with experimental data for NPR=4 with 3% injection, θ_1=-10 degrees.

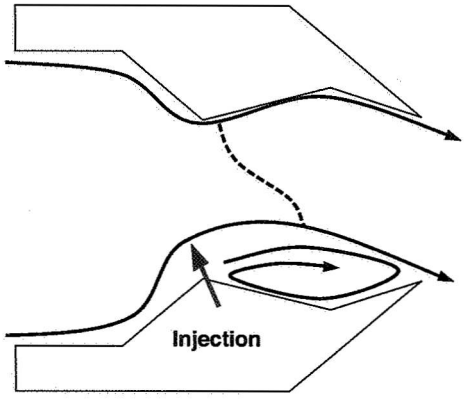

Figure 1. Sketch of the dual throat fluidic thrust vectoring nozzle

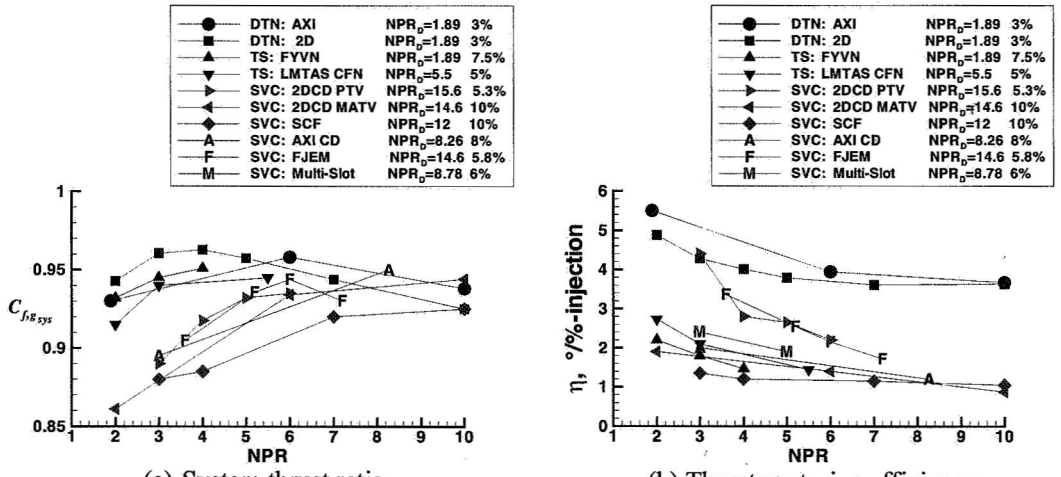

(a) System thrust ratio (b) Thrust vectoring efficiency

Figure 2. Comparison of nozzle performance for several fluidic injection techniques; dual throat nozzle (DTN), throat-shifting (TS), and shock vector control (SVC) nozzles.

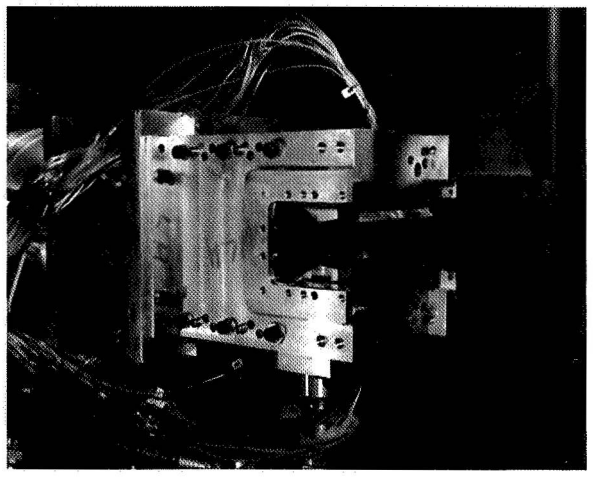

Figure 3. The NASA Langley Research Center Dual Throat Fluidic Thrust Vectoring nozzle installed in the Jet Exit Test Facility

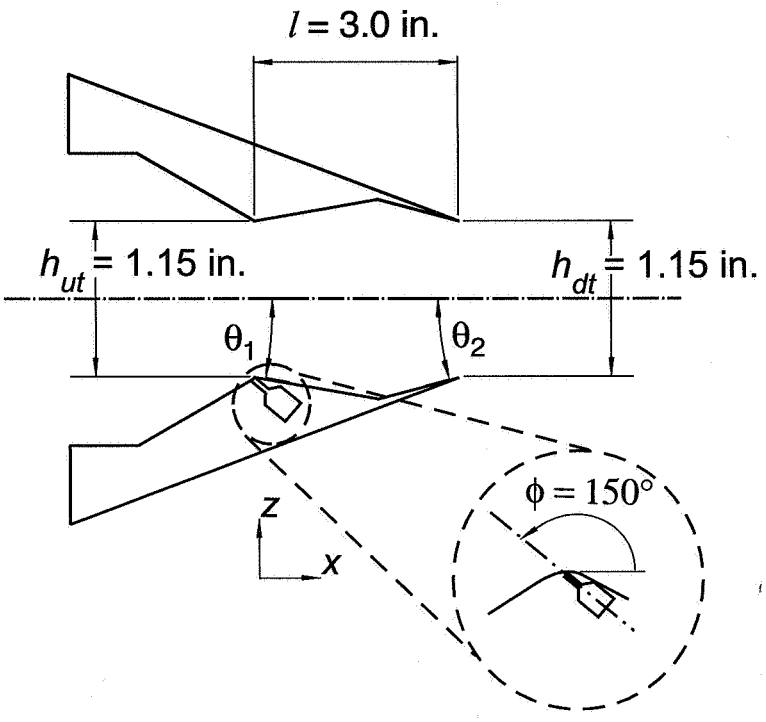

Figure 4. Sketch illustrating the geometric design variables for the Dual Throat Fluidic Thrust Vectoring Nozzle (not to scale).

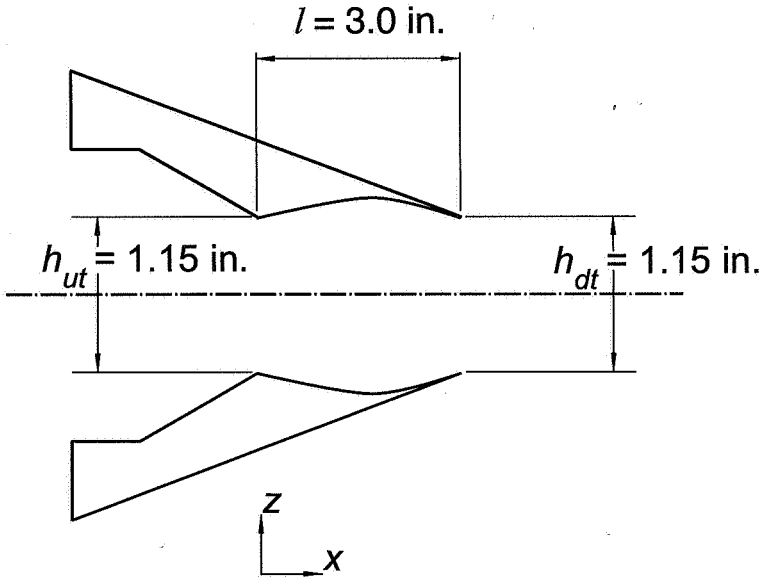

Figure 5. Sketch of 2D Dual Throat FTV nozzle with curved cavity (not to scale).

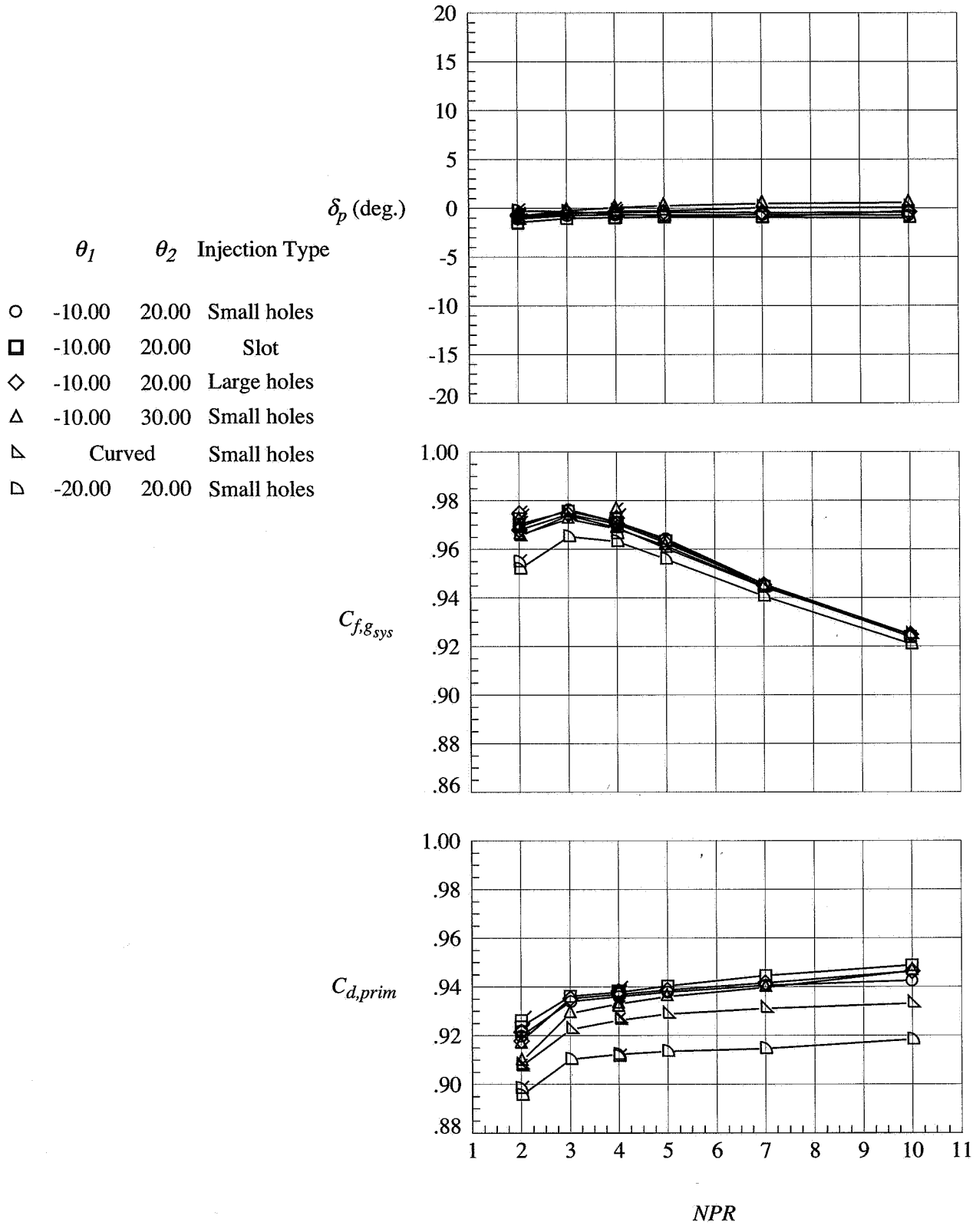

Figure 6. Nozzle performance without secondary injection as a function of NPR. Note: flagged symbols indicate data taken in descending order

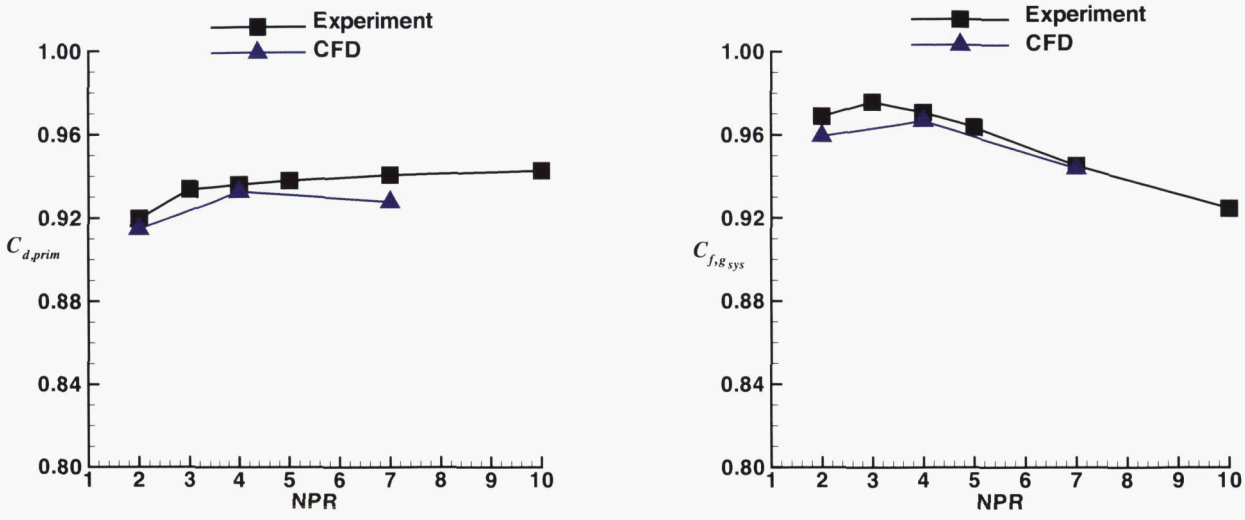

(a) Primary discharge coefficient

(b) Resultant thrust ratio

Figure 7. Comparison of experimental and computational nozzle performance with no secondary injection, $\theta_1 = -10°$, $\theta_2 = 20°$.

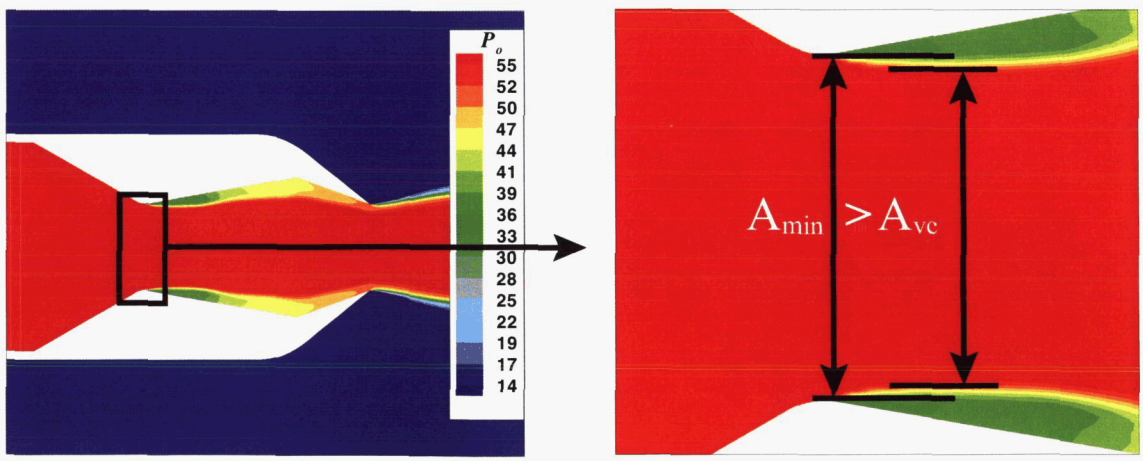

(a) Full view of primary flow through nozzle geometry (white).

(b) Enlarged view of upstream throat.

Figure 8. Computational total pressure flow contours show the decreased effective area (A_{vc}) from the vena-contracta effect at the upstream minimum area (A_{min}).

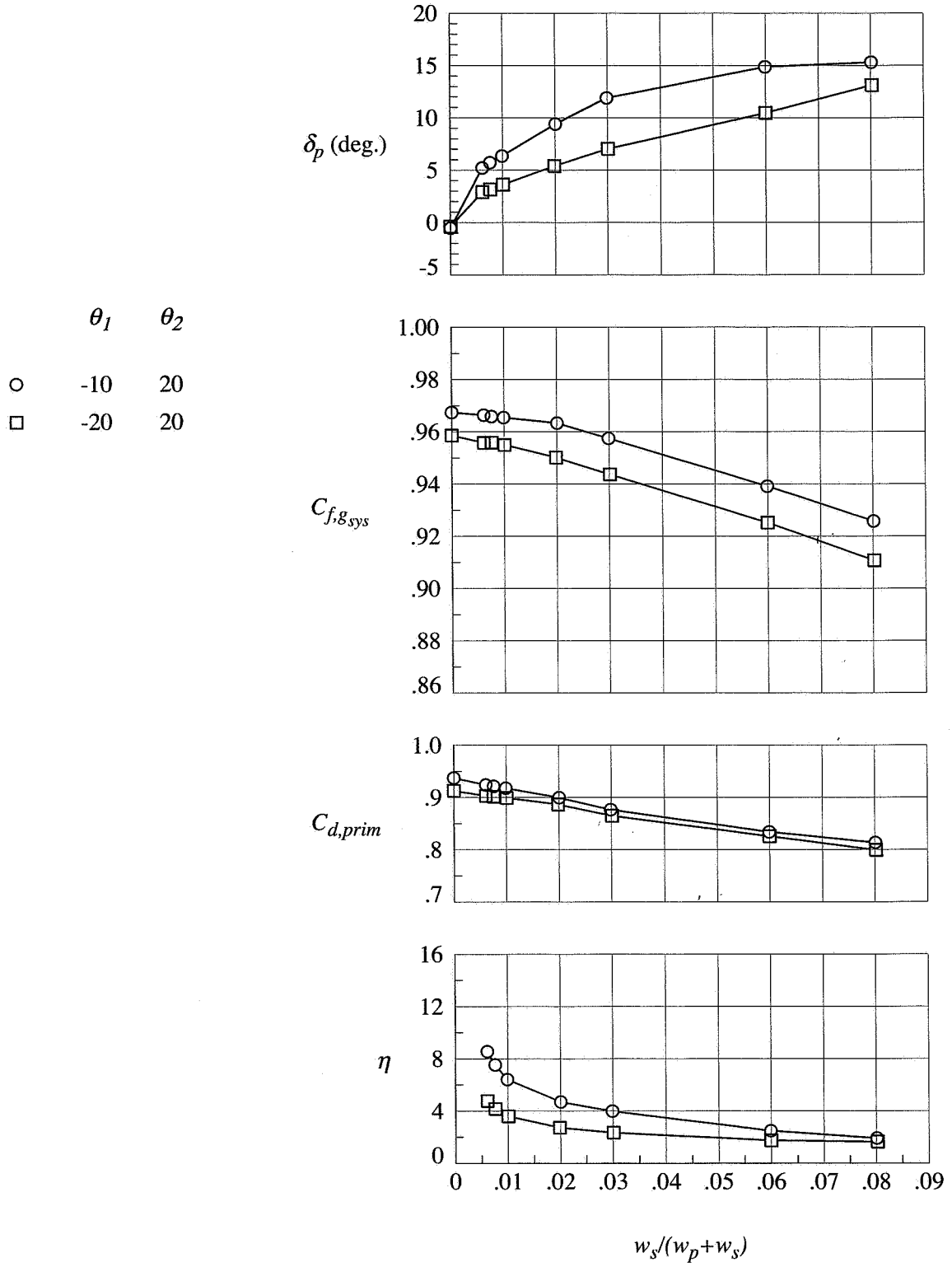

Figure 9. Effect of divergent cavity ramp angle θ_1: NPR = 4.00, $\theta_2 = 20°$.

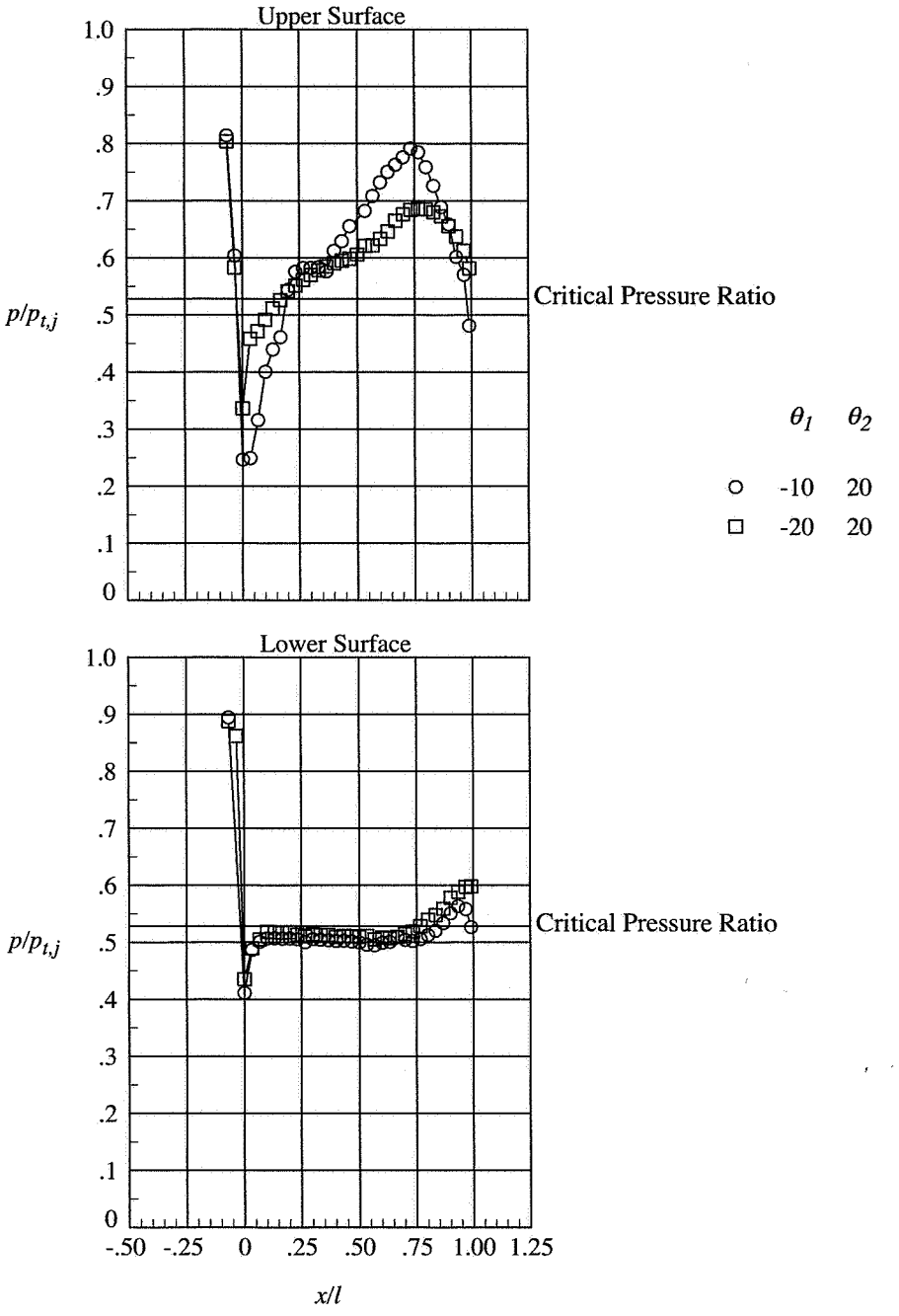

Figure 10. Effect of divergent cavity ramp angle θ_1 on nozzle centerline pressures: NPR = 4.00, $w_s/(w_s+w_p) = 0.03$, $\theta_2 = 20°$.

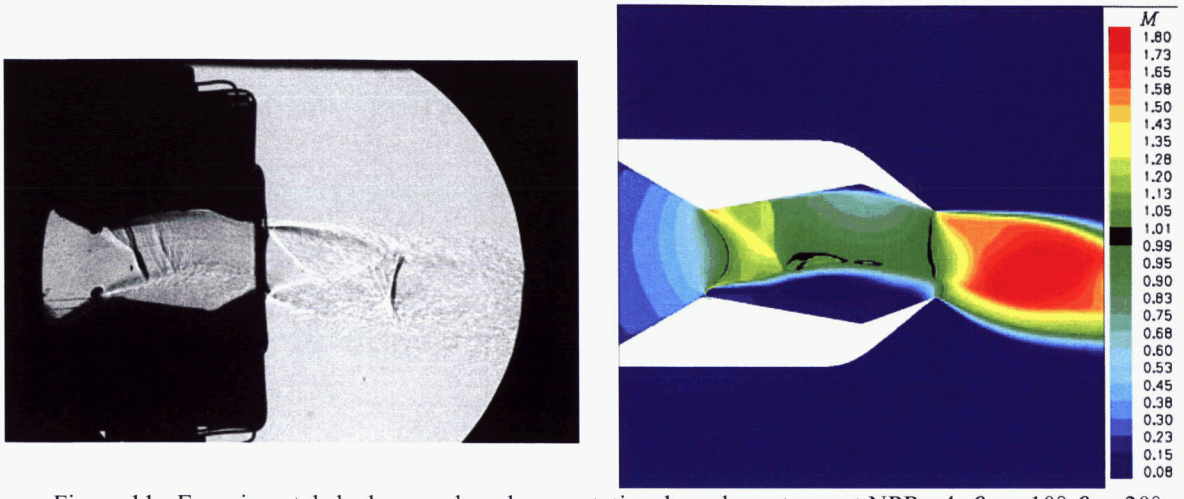

Figure 11. Experimental shadowgraph and computational mach contours at NPR =4, $\theta_1 = -10°, \theta_2 = 20°$, $w_s/(w_s+w_p) = 0.03$.

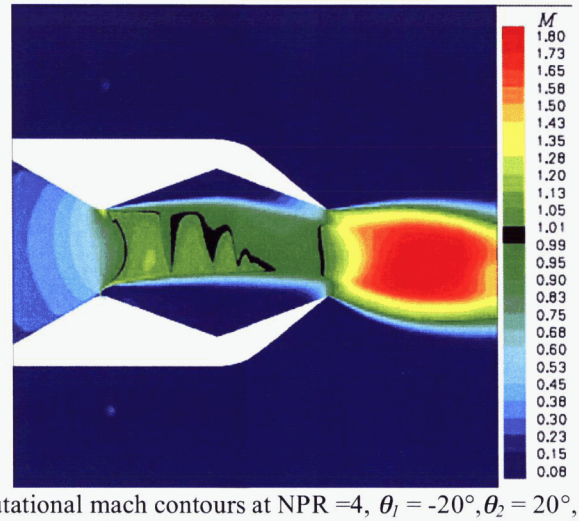

Figure 12. Computational mach contours at NPR =4, $\theta_1 = -20°, \theta_2 = 20°$, $w_s/(w_s+w_p) = 0.03$.

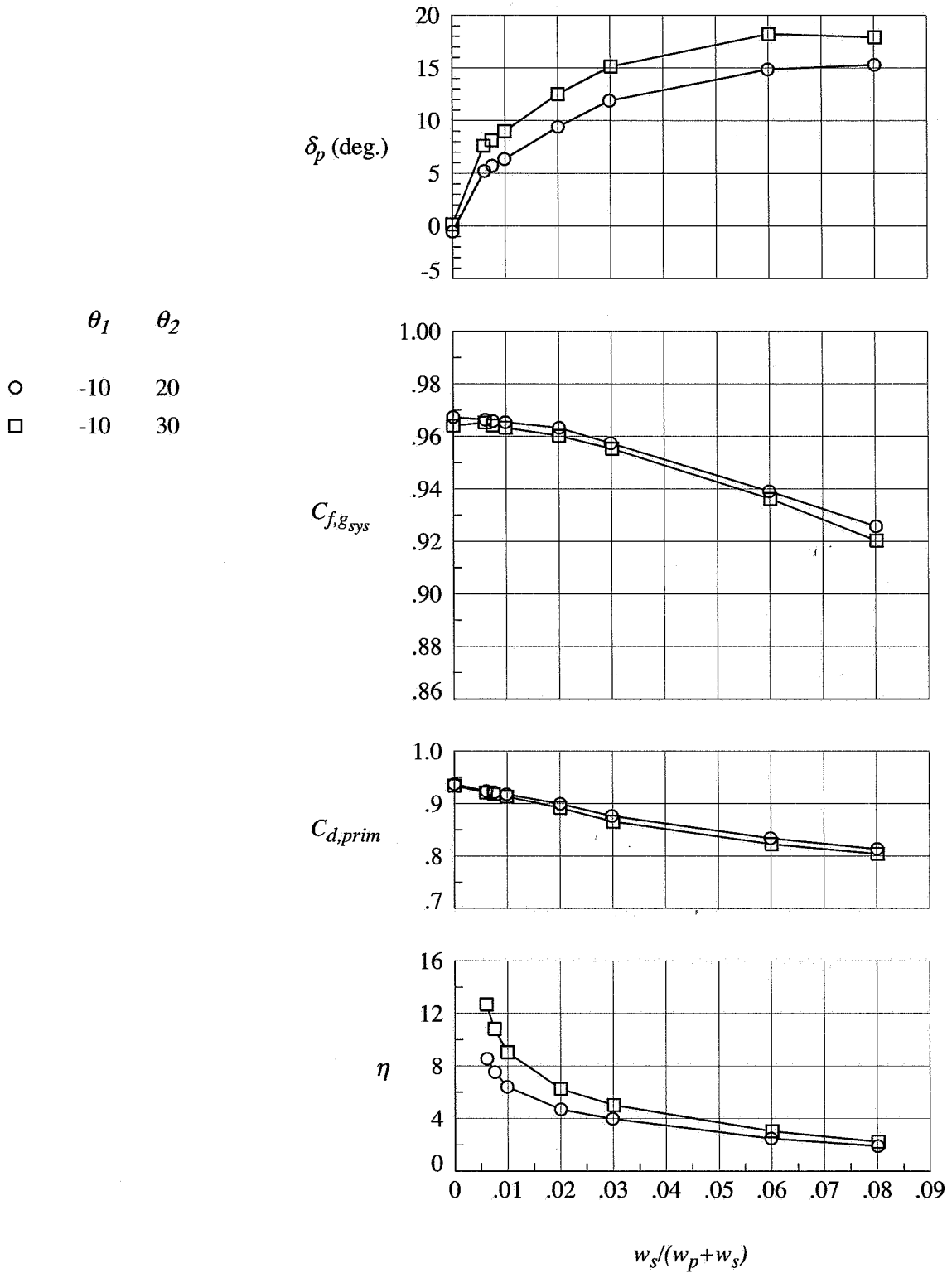

Figure 13. Effect of convergent cavity ramp angle θ_2: NPR = 4.00, θ_1 = -10°.

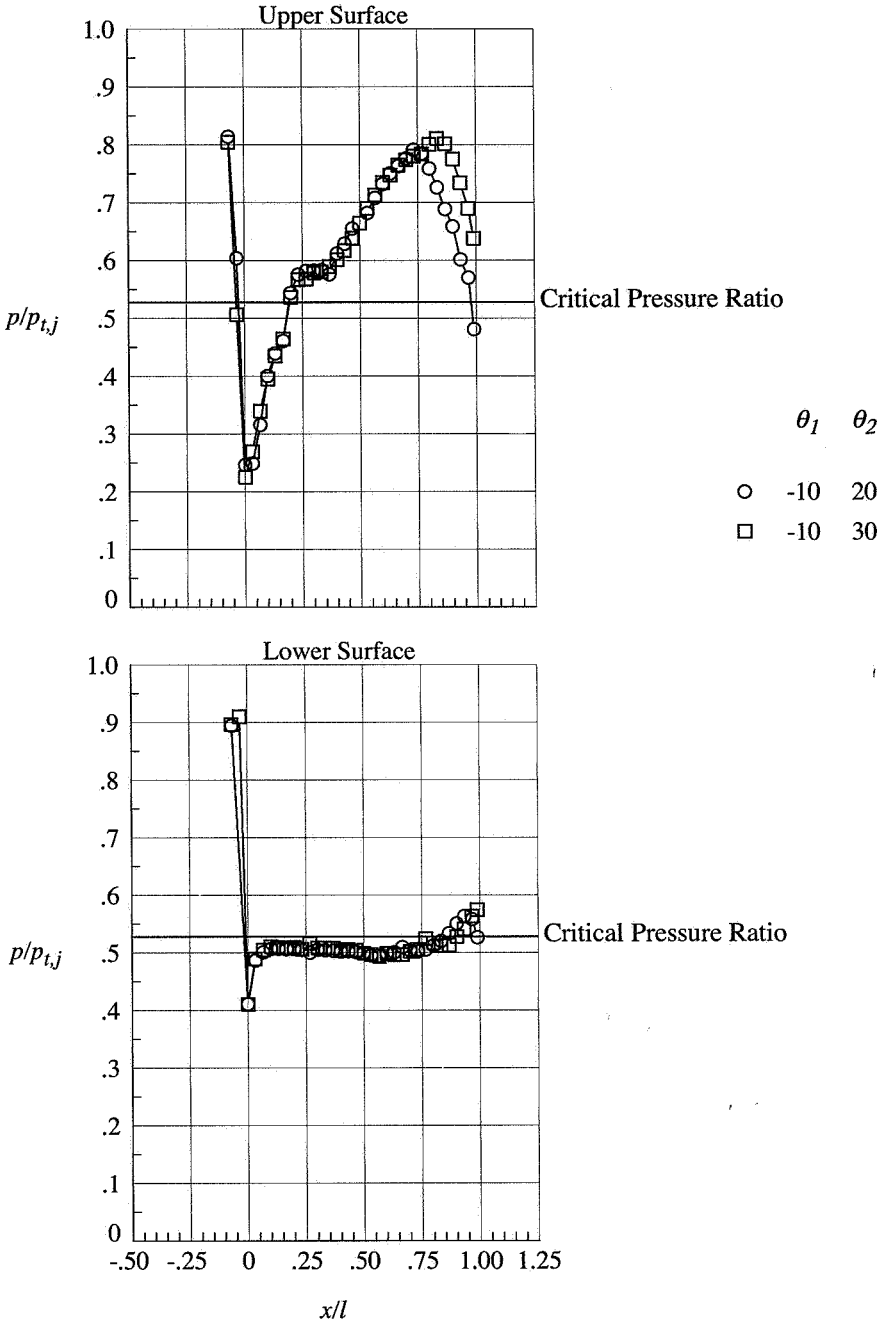

Figure 14. Effect of convergent cavity ramp angle θ_2 on nozzle centerline pressures: NPR = 4.00, $w_s/(w_s+w_p) = 0.03$, $\theta_1 = 10°$.

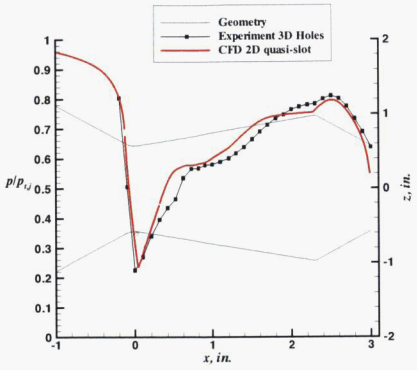

(a) Upper-wall pressure distributions

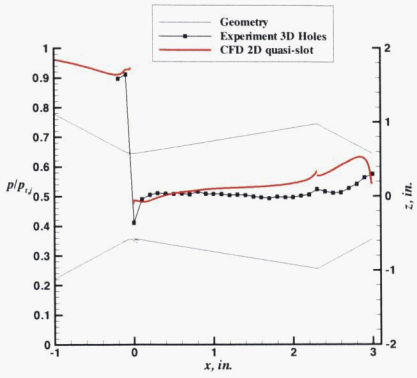

(b) Lower-wall pressure distributions

Figure 15. Comparison of experimental pressure distributions with CFD prediction: NPR = 4.00, 3%-injection, θ_1= - 10°, θ_2 = 30°.

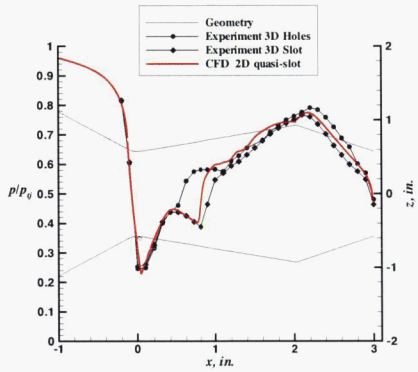

(a) Upper-wall pressure distributions

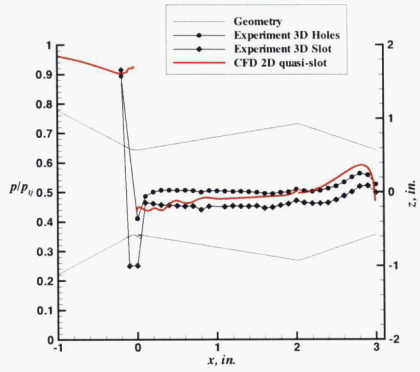

(b) Lower-wall pressure distributions

Figure 16. Comparison of experimental pressure data with CFD prediction: NPR = 4.0, 3%-injection, θ_1= -10°, θ_2 = 20°.

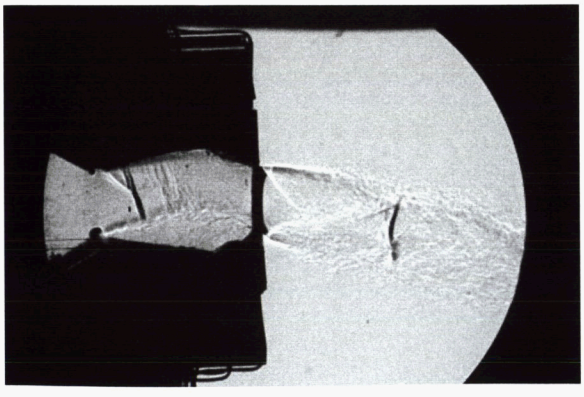

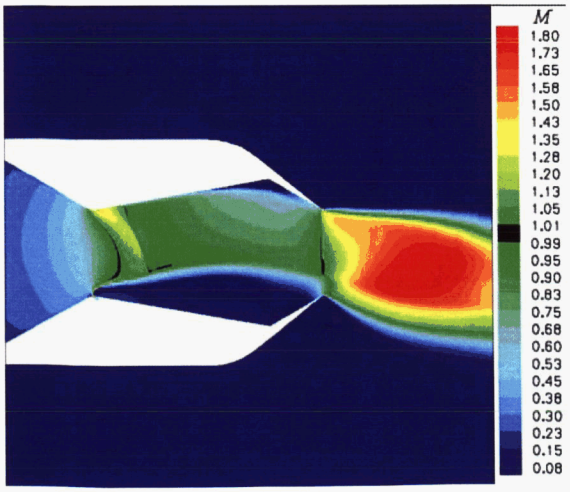

Figure 17. Experimental shadowgraph and computational mach contours at NPR =4.0, θ_1 = -10°,θ_2 = 30°, $w_s/(w_s+w_p)$ = 0.03.

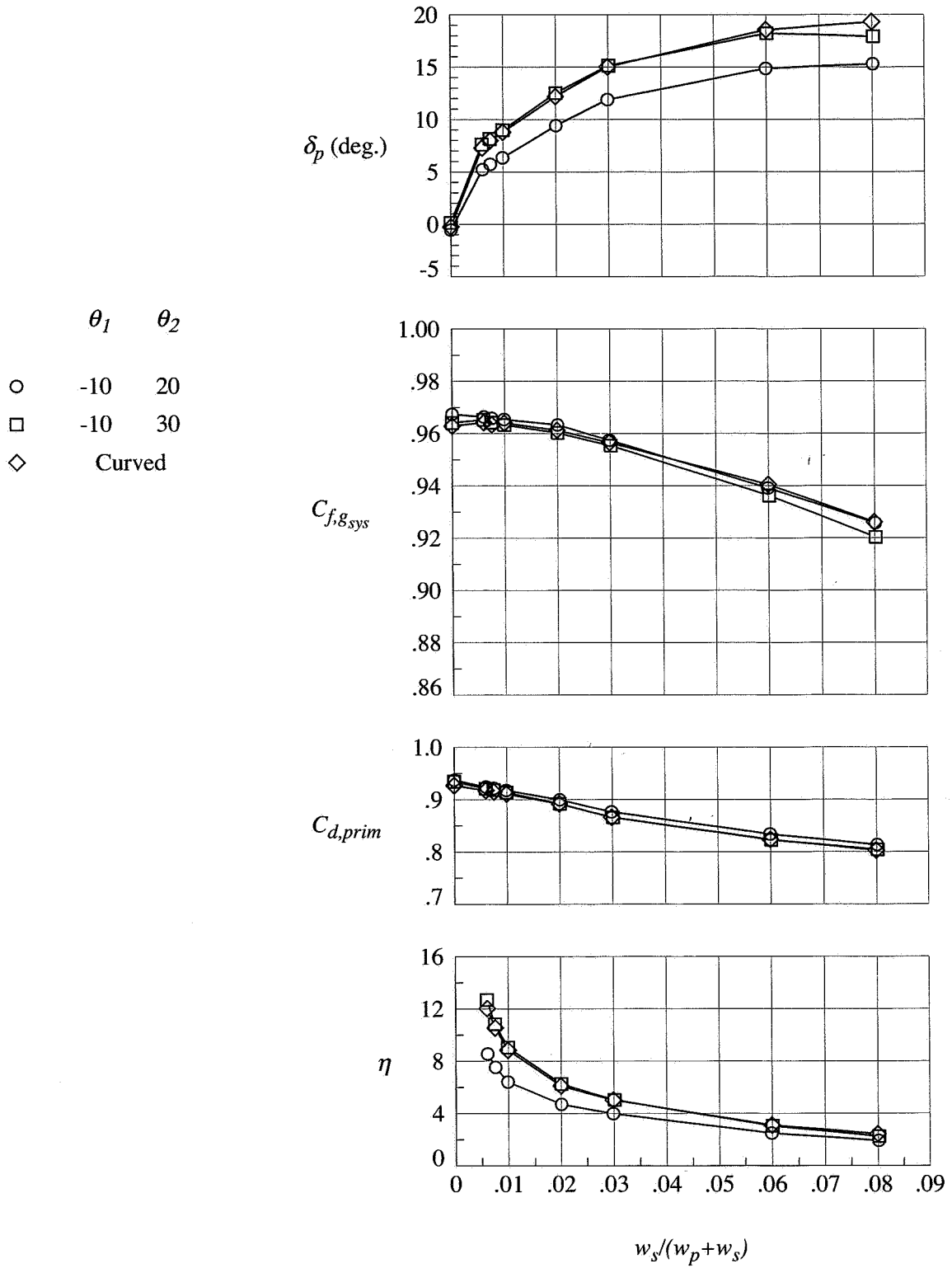

Figure 18. Effect of cavity shape: NPR = 4.0.

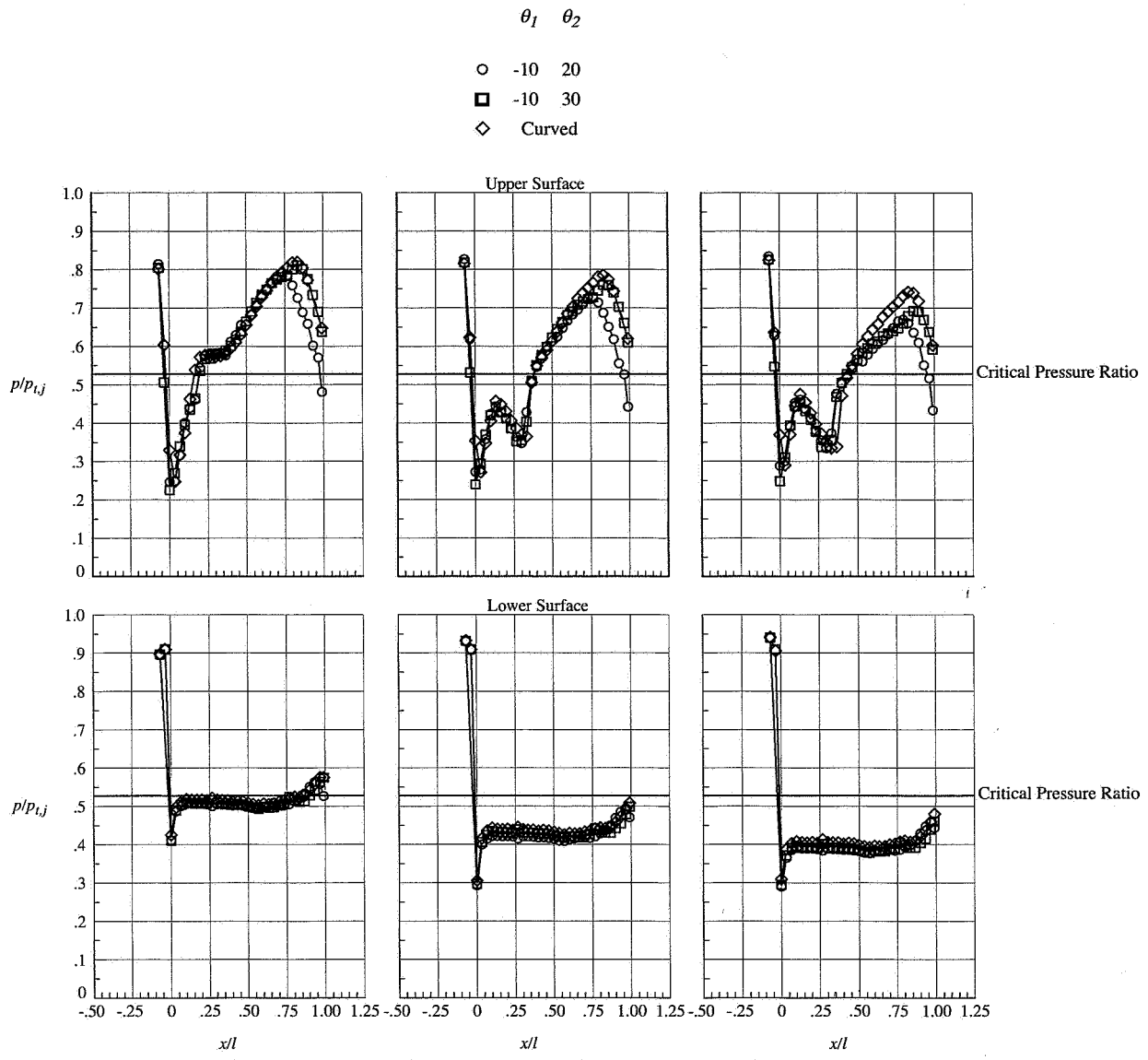

Figure 19: Effect of cavity shape on nozzle centerline pressures, NPR = 4.0.

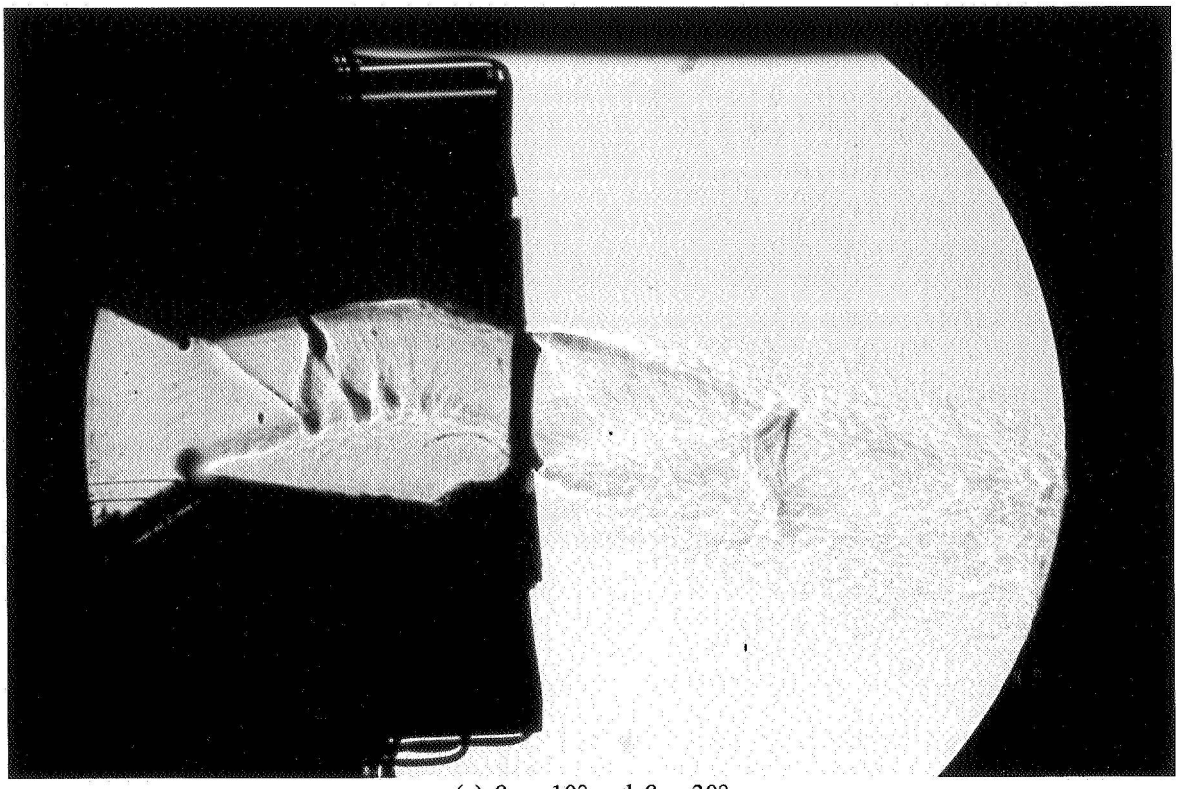

(a) $\theta_1 = -10°$ and $\theta_2 = 30°$

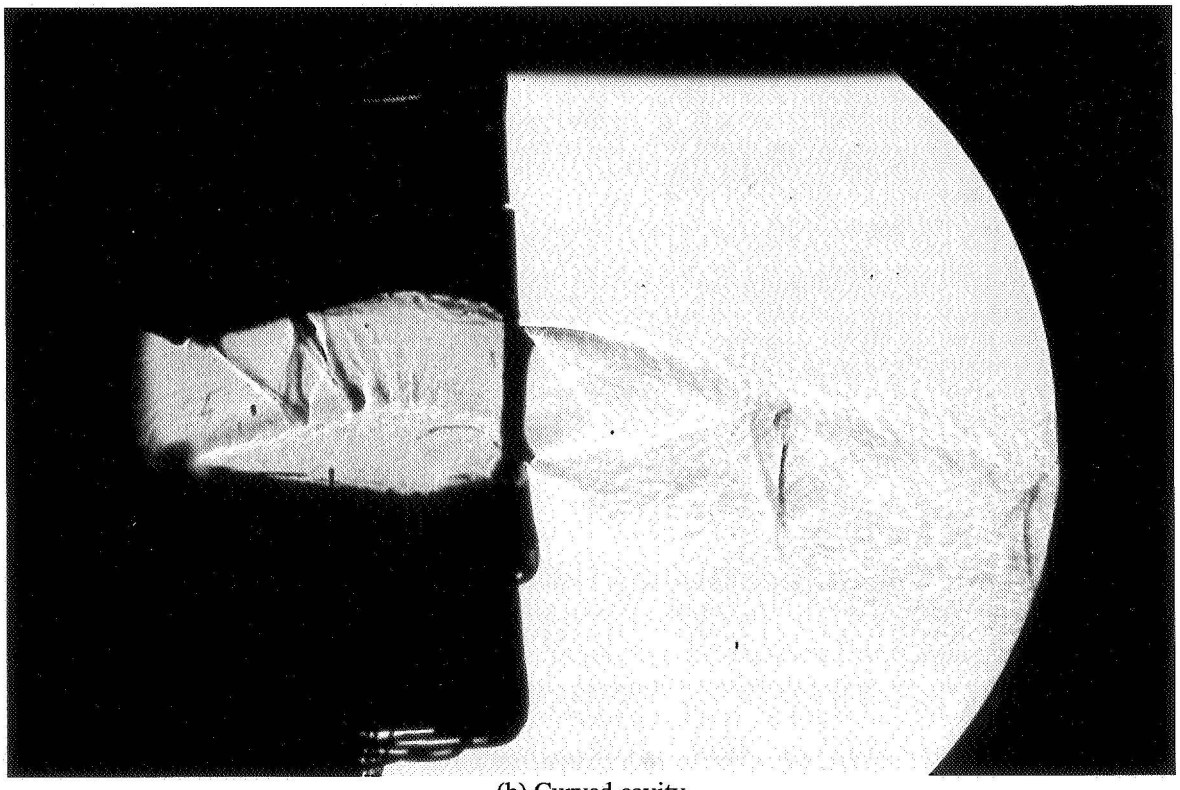

(b) Curved cavity

Figure 20. Experimental shadowgraph images showing effect of cavity shape: NPR = 4.0, 6% secondary injection.

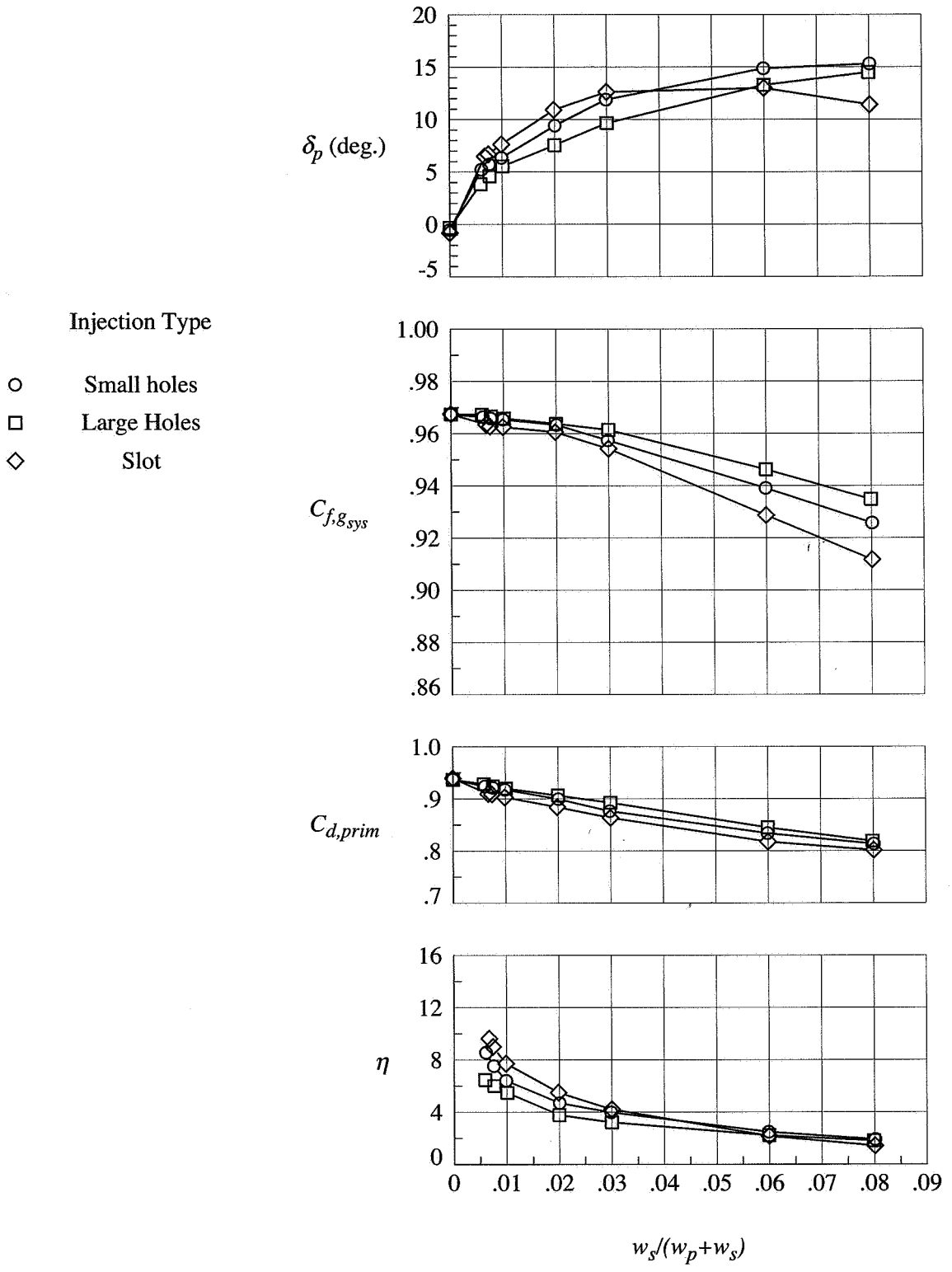

Figure 21. Effect secondary injection geometry: NPR = 4.0, θ_1=-10°, θ_2 = 20°.

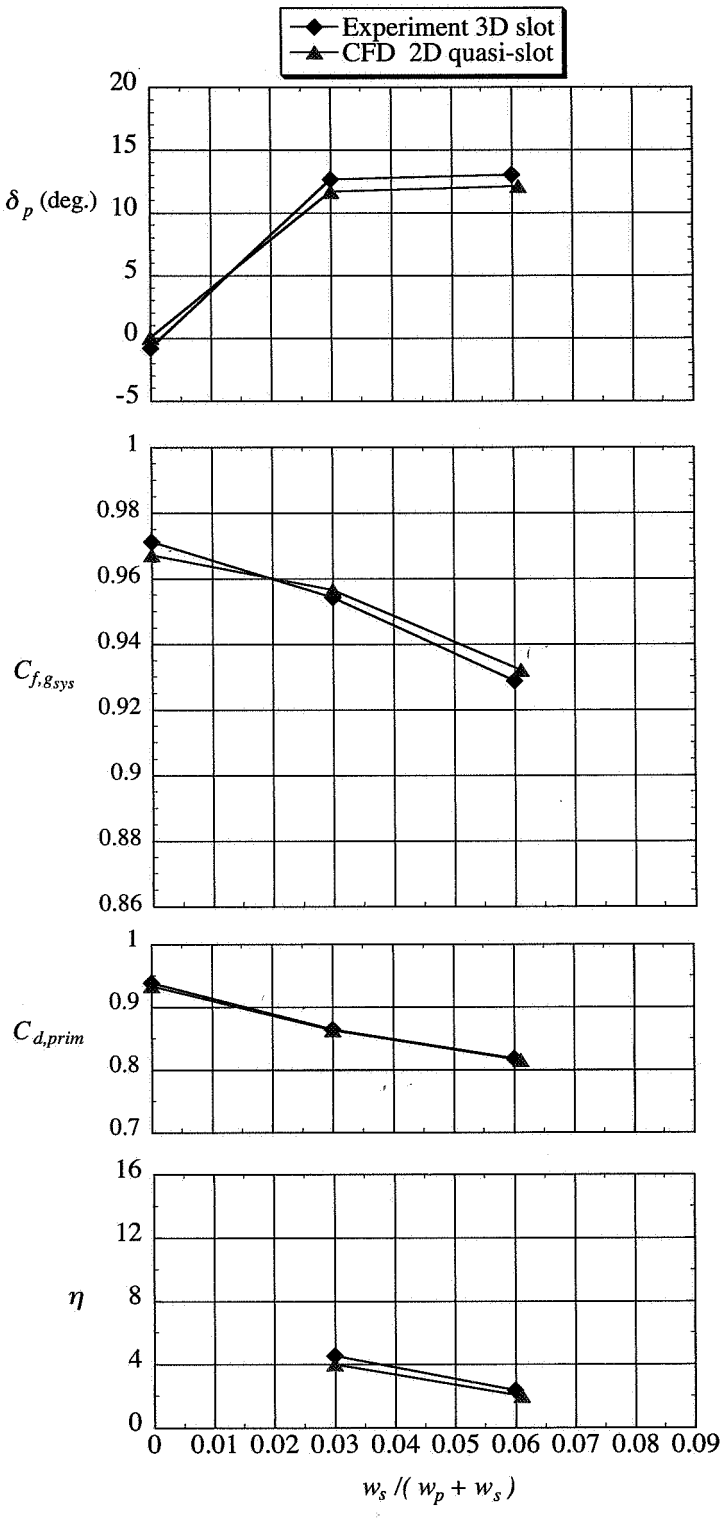

Figure 22. Comparison of experimental data with CFD prediction for slot injection: NPR = 4.0, θ_1=-10°, θ_2 = 20°.